VIP neurons desynchronize cortical assemblies

Julia Veit[1*†], Daniel P. Mossing[1,3] Hillel Adesnik[1,2†]
[1]Department of Molecular and Cell Biology, University of California, Berkeley
[2]The Helen Wills Neuroscience Institute, University of California, Berkeley
[3]Biophysics Graduate Program, University of California, Berkeley
[*]Present address: Department of Physiology, University of Freiburg, Freiburg, Germany
[†]Corresponding authors: julia.veit@physiologie.uni-freiburg.de, hadesnik@berkeley.edu

Abstract

Neural synchronization on fast timescales has been linked to critical aspects of sensation, cognition and action, and impairments in synchronization are associated with neurological disease. Although the strength and spatial scale of neural synchronization varies dramatically with sensory and behavioral context, the circuit mechanisms that regulate the magnitude and spatial spread of neural oscillations are largely unknown. As in humans, monkeys, and cats, we found that in the mouse primary visual cortex (V1) the stimulus properties and behavioral state powerfully modulate gamma band synchronization. To reveal the underlying circuit that mediates this dependence, we used multi-site multi-electrode electrophysiology and cell type specific optogenetic suppression of vasoactive intestinal peptide (VIP) interneurons in awake mice. Our results show that VIP neurons potently control the gain and behavioral state-dependence of gamma band network synchronization by desynchronizing local and global networks on fine time scales. Importantly, VIP neurons preferentially decouple spatially separated cortical ensembles when they are processing non-matched stimulus features. Based on these data, we propose that cortical disinhibition by VIP interneurons fine-tunes the strength and spatial architecture of gamma-oscillating neural assemblies, which may facilitate the downstream generation of coherent visual percepts.

Introduction

Synchronized activity is widespread in neural systems, occurring both spontaneously and during sensory stimulation, cognition, and motor action (Jasper & Penfield, 1949; Adrian, 1950; Bressler & Freeman, 1980; Riehle *et al.*, 1997; Buzsáki & Draguhn, 2004; Colgin *et al.*, 2009; Fries, 2009). In monkeys, synchronization is dependent on stimulus features (Gieselmann & Thiele, 2008; Ray & Maunsell, 2010; Ray *et al.*, 2013) and modulated by behavioral state, such as directed attention (Fries *et al.*, 2001; Womelsdorf & Fries, 2006; Chalk *et al.*, 2010; Vinck *et al.*, 2013). Synchronization may facilitate neural communication by enhancing the temporal co-incidence of synaptic excitatory potentials in target neurons (Colgin *et al.*, 2009; Fries, 2015). Conversely, excessive synchrony may also limit information carrying capacity of neural networks (Benda *et al.*, 2006). Thus, both too much or too little synchrony could degrade cortical communication and lead to neurological disorders (Lewis *et al.*, 2005; Schnitzler & Gross, 2005; Uhlhaas & Singer, 2010; Yizhar *et al.*, 2011). Therefore, understanding the cellular mechanisms that precisely regulate the strength and specificity of oscillations is crucial to determining their role in brain function and disease. Remarkably, despite detailed knowledge of the phenomenology of cortical oscillations on one hand, and a deep mechanistic and theoretical insight into their underlying synaptic basis on the other (Traub *et al.*, 2004; Bartos *et al.*, 2007; Buzsáki & Wang, 2012) we have a very limited understanding for the neural circuits that regulate their magnitude across different sensory and behavioral contexts (Fries *et al.*, 2001; Chalk *et al.*, 2010).

Mechanistically, ample evidence indicates that local GABAergic interneurons temporally entrain excitatory neurons by biasing their spike timing to the trough of their periodic inhibitory synaptic potentials (Bartos *et al.*, 2002, 2007; Hasenstaub *et al.*, 2005, 2016; Tukker *et al.*, 2007; Wulff *et al.*, 2009; Buzsáki & Wang, 2012; Perrenoud *et al.*, 2016; Zhang *et al.*, 2018). This periodicity results from the recurrent interaction between excitatory and inhibitory neurons (Hasenstaub *et al.*, 2005), through direct interneuron-to-interneuron synaptic coupling (Sohal & Huguenard, 2005), and through electrical synapses (Traub *et al.*, 2001; Long *et al.*, 2005; Neske & Connors, 2016). Cortical gamma oscillations depend on various types of interneurons, including soma-targeting parvalbumin positive basket cells (Cardin *et al.*, 2009; Sohal *et al.*, 2009). In the mouse primary visual cortex, a visually induced gamma oscillation (25-40 Hz), similar to the widely studied gamma rhythms in higher mammals, requires the activity of somatostatin (SST) interneurons (Adesnik *et al.*, 2012; Chen *et al.*, 2017; Veit *et al.*, 2017; Hakim *et al.*, 2018). In V1, SST neuron firing rates strongly correlate with visually induced narrow-band gamma power on a trial-to-trial basis, and optogenetic inactivation of SST neurons (but not PV neurons) nearly abolishes visually evoked gamma oscillations (Veit *et al.*, 2017). SST neurons are also known to be critical for the encoding of contextual stimuli, such as for gratings that extend beyond neurons' classical receptive fields (Adesnik *et al.*, 2012; Nienborg *et al.*, 2013; Keller, Dipoppa, *et al.*, 2020; Mossing *et al.*, 2021). Notably, a second narrowband gamma oscillation around ~60 Hz that is increased by locomotion, but strongly suppressed by visual stimuli, is also present in V1 but is not of cortical origin (Saleem *et al.*, 2017; Storchi *et al.*, 2017; Veit *et al.*, 2017; Hoseini *et al.*, 2021). This oscillation is not the focus of this study.

The recent discovery that VIP interneurons preferentially inhibit other interneurons, especially SST neurons, (Pfeffer *et al.*, 2013; Pi *et al.*, 2013; Karnani, Jackson, Ayzenshtat, Hamzehei Sichani, *et al.*, 2016) raises the hypothesis that they might regulate the strength of gamma band oscillations. Furthermore, since VIP neurons are strongly implicated in brain state-dependent changes in cortical gain (Lee *et al.*, 2013; Fu *et al.*, 2014; Dipoppa *et al.*, 2018) they might simultaneously be crucial for the behavioral dependence of cortical synchronization (Niell & Stryker, 2010). Acetylcholine is a known regulator of gamma band power in midbrain structures (Bryant *et al.*, 2015), hippocampus (Betterton *et al.*, 2017) and the cortex (Bhattacharyya *et al.*, 2013; Howe *et al.*, 2017), and VIP neurons are potently driven by acetylcholine (Fu *et al.*, 2014; Askew *et al.*, 2019) and may co-release it (Eckenstein & Baughman, 1984; Dudai *et al.*, 2020; Granger *et al.*, 2020). Genetic mutations that reduce VIP neuron activity dramatically alter the temporal structure of spontaneous activity in mouse V1, degrade visual stimulus selectivity, and impair sensory learning (Batista-Brito *et al.*, 2017). Remarkably, selective deletion of the transcriptional regulator *MECP2* in VIP neurons, the gene whose mutation results in Rett syndrome, also substantially alters cortical dynamics and behavior, further linking specific dysfunctions in VIP circuitry to neurological disease (Mossner *et al.*, 2020).

Acute pharmacogenetic suppression of VIP neurons in mouse V1 reduces network activity across brain states, and alters visual responses (Ayzenshtat *et al.*, 2016; Jackson *et al.*, 2016; Keller, Dipoppa, *et al.*, 2020). VIP neurons appear to work co-operatively as inhibitory subnetworks to control population level activity, and select active excitatory ensembles through local disinhibition (Karnani, Jackson, Ayzenshtat, Hamzehei Sichani, *et al.*, 2016). Remarkably, optogenetic stimulation of VIP neurons is sufficient to drive operant responses in mice performing a contrast detection task (Cone *et al.*, 2019). In multiple cortical areas, VIP activity correlates with reinforcement signals (Pi *et al.*, 2013). VIP neurons in the sensory cortex are also major targets of 'top-down' cortico-cortical axons (Zhang *et al.*, 2014), which often convey contextual information (Keller, Roth, *et al.*, 2020) and therefore are plausibly poised to regulate the inter-areal communication and synchrony potentially involved in driving sensory perception (Lee *et al.*, 2013; Zhang *et al.*, 2014; Wall *et al.*, 2016). Finally, recent work has shown that VIP neurons are suppressed by visual stimuli (Keller, Dipoppa, *et al.*, 2020; Millman *et al.*, 2020; Mossing *et al.*,

2021) that have previously been shown to drive strong gamma oscillations (Gieselmann & Thiele, 2008; Ray *et al.*, 2013; Veit *et al.*, 2017), but no direct link has been established.

Although these studies collectively support a crucial role of VIP neurons in multiple aspects of visual computation, perception and behavior, it remains unclear whether VIP neurons might regulate fast temporal dynamics in the cortex. Based on all the features of gamma oscillations in V1 and the circuit properties of VIP neurons, especially their selective inhibition of other interneurons involved in gamma oscillations, we hypothesized that VIP neurons should play a critical role in regulating the stimulus and behavioral-state dependence of local and long-range synchronization in V1. More specifically, we hypothesized that VIP activity desynchronizes V1 assemblies.

First, we confirmed that in mice the strength of visually induced gamma oscillations in V1 depends profoundly on the size, contrast and global statistical properties of visual stimuli. Next, we found that high VIP activity correlates with desynchronized network states, while high activity of SST neurons correlates with synchronized states. To causally probe this relationship, we found that optogenetically suppressing VIP neurons potently enhances gamma band power and the phase locking of single units across stimulus contrast, size, and the relative orientation between the center and surround of large gratings. Furthermore, we found that the desynchronizing action of VIP neurons depends on the behavioral state, helping to temporally decorrelate neural ensembles during locomotion. Finally, we discovered that VIP neurons preferentially decouple spatially distinct networks in V1 that are processing stimuli of orthogonal orientations, suggesting a neural circuit mechanism that may contribute to feature-dependent sensory binding. These widespread effects of VIP neuron suppression might help explain why perturbation of VIP neurons – whether it be genetically, pharmacologically, or optogenetically – potently impairs visual behaviors and learning. Furthermore, they raise the notion that developmental defects in VIP neurons might lead to a range of neurological disorders that have been linked to changes in cortical rhythms, potentially throuogh maladaptive hypersynchronization.

Results

Dynamic, stimulus-dependent gamma band synchronization in the mouse primary visual cortex

In primates, cats, and humans, visual stimuli can induce potent oscillations in the gamma band (20-90 Hz), yet the strength of these rhythms depends on the properties of the visual stimulus (Gray *et al.*, 1989; Gieselmann & Thiele, 2008; Ray & Maunsell, 2010; Hermes *et al.*, 2015; Self *et al.*, 2016; Bartoli *et al.*, 2019; Peter *et al.*, 2019) and the brain state (Chalk *et al.*, 2010; Bosman *et al.*, 2012). To probe this dependence in mouse primary visual cortex (V1), we presented head-fixed, awake, locomoting mice with drifting gratings varying in size, contrast, or the orientation of the grating surround relative to the center. We inserted one or two laminar multielectrode arrays into the superficial layers of the primary visual cortex to record both isolated single units and the local field potential (LFP) (Fig. 1A). As previously reported, visual stimuli potently and specifically induced narrow band gamma oscillations (~30 Hz) for the duration of the stimulus (Fig. 1,B-D). Consistent with prior work on visually induced gamma oscillations, we found that gamma power, as measured in the LFP, rose monotonically with stimulus contrast or size, showing a nearly 5-fold enhancement between the lowest and highest contrast (at the largest size), and a 3-fold enhancement between the smallest and largest size (at full contrast) (Fig. 1E-F). Conversely, gamma power decreased as the relative angle of orientation between the center and surround was increased (~1.4 fold increase from cross-oriented to iso-oriented) (Fig. 1G).

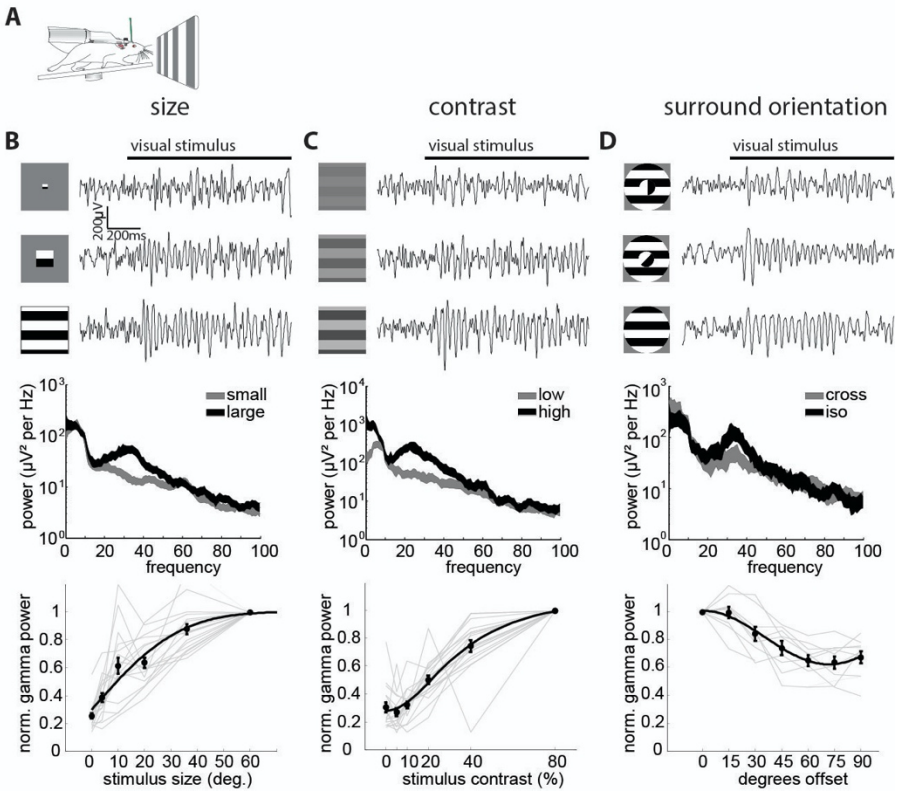

Figure 1. Stimulus dependence of the visually induced gamma rhythm in V1 of awake, running mice. A: Experimental schematic of a head-fixed mouse on a running wheel facing a screen for visual stimulation. **B:** Top: three example LFP traces filtered between 10 and 90 Hz in response to a small (4˚, top), medium (20˚, middle) and large (60˚, bottom) drifting grating (temporal frequency, 2 Hz). Middle: example LFP power spectrum in response to a small (4˚) and large (60˚) drifting grating (thickness of line denotes mean ± standard error). Bottom: Plot of normalized peak gamma power (peak frequency: 28.8±0.5 Hz) versus stimulus size (Kruskal-Wallis ANOVA: $p < 0.0001$, n = 17) **C:** Top: three example filtered LFP traces in response to a low (5%, top), medium (20%, middle) and high (80%, bottom) contrast drifting grating. Middle: example LFP power spectrum in response to low (5%) and high (80%) contrast gratings (thickness of line denotes mean ± standard error). Bottom: Plot of normalized peak gamma power (peak frequency: 27.3±0.6 Hz) versus stimulus contrast (Kruskal-Wallis ANOVA: $p<0.0001$, n = 18). **D:** Top: three example filtered LFP traces in response to a grating with cross- (90˚ offset, top), intermediate- (45˚ offset, middle) and iso-oriented (0˚ offset, bottom) surround relative to the center. Middle: Example LFP power spectrum in response to iso and cross oriented surround grating (thickness of line denotes mean ± standard error). Bottom: Plot of normalized peak gamma power (peak frequency: 32.8±0.4 Hz) versus stimulus contrast (Kruskal-Wallis ANOVA: $p<0.0001$, n = 10). Error bars in all plots represent s.e.m.

To test whether these gamma oscillations are directly linked to the entrainment of spiking in V1, we measured the phase locking of spikes to the LFP gamma oscillation (computed via the pairwise phase consistency, 'PPC' (Vinck *et al.*, 2010)) for each recorded unit. Most units (96/126 for a large grating) showed a significant bias to fire at certain phases of the gamma cycle (Fig. 2A). We categorized units as either regular spiking or fast spiking (see Methods) and found that both populations strongly and specifically coupled to the LFP gamma oscillation in a manner depending on the size, contrast, and relative orientation of the stimulus center/surround (Figure 2B-D). These data demonstrate that in mouse V1, just as in higher mammalian species, the strength of gamma oscillations and the network synchronization of cortical neurons is strongly feature-dependent.

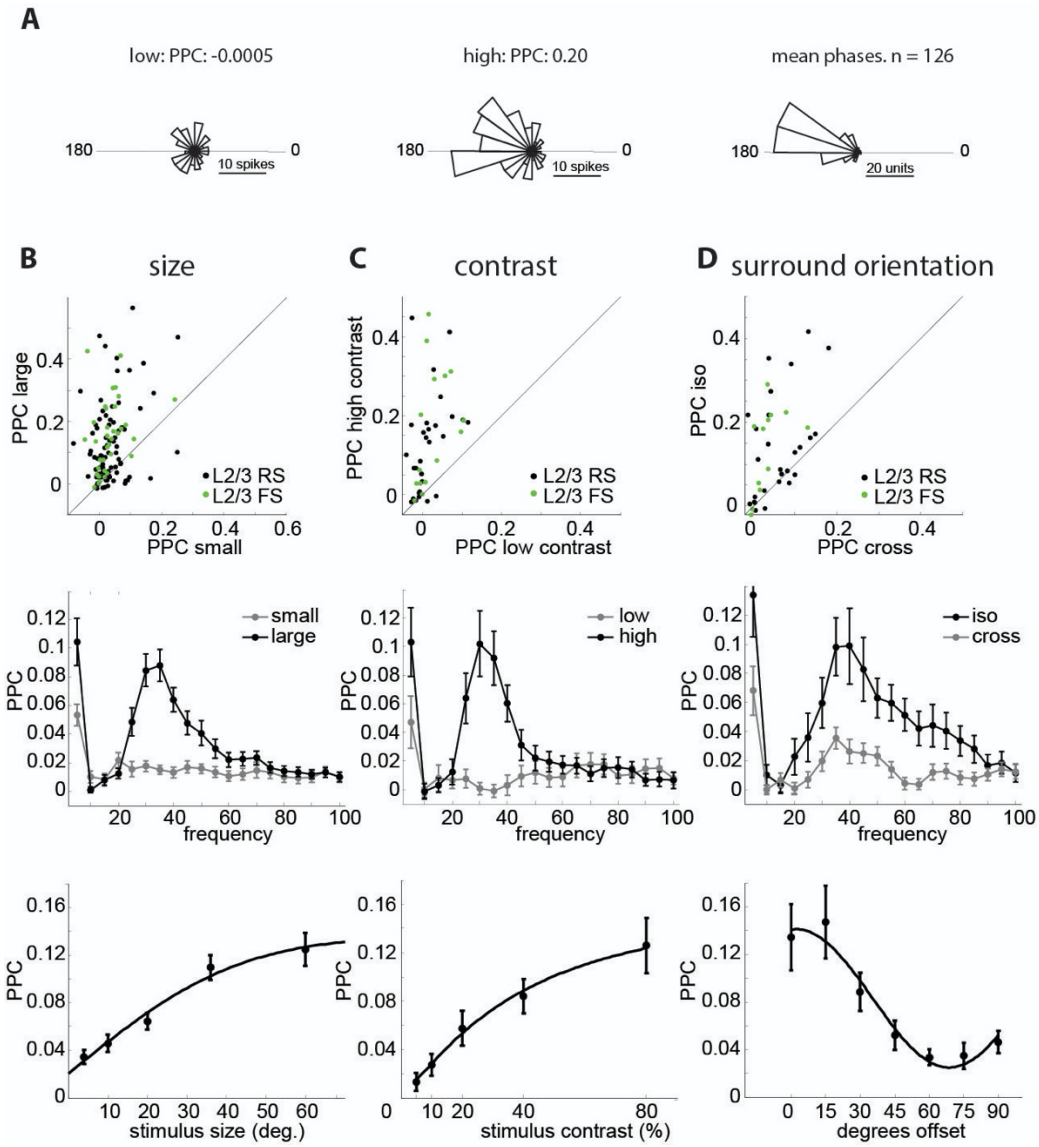

Figure 2: Single units lock to visually induced gamma oscillations in a stimulus-dependent manner. A: Left: phase histogram of the spikes of an example L2/3 RS unit relative to the gamma oscillation in response to a low contrast (5%) stimulus. Middle: similar histogram from the spikes of the same neuron evoked by ahigh contrast (80%) stimulus. Right: histogram of the average spike phases of all 126 included L2/3 RS cells included for a large high contrast grating. Cells tend to fire shortly before the trough of the oscillation (180˚). **B:** Top: scatter plot of PPC values for single RS (black, n = 78, p<0.0001, Wilcoxon signed rank test) and FS (green, n = 32, p<0.0001, Wilcoxon signed rank test) units in response to small (4˚) and large (60˚) full contrast stimuli. Middle: average PPC spectra for L2/3 RS cells (n = 78) for small (gray, 4˚) and large (black, 60˚) full contrast stimuli. Bottom: Plot of average PPC at individual gamma center frequency versus stimulus size for L2/3 RS units (n = 87, p < 0.0001 , Kruskal-Wallis ANOVA). **C:** Top: scatter plot of PPC values for single RS (black, n = 29, p<0.0001, Wilcoxon signed rank test) and FS (green, n = 15, p<0.0001, Wilcoxon signed rank test) units in response to large low (5%) and high (80%) contrast stimuli. Middle: average PPC spectra for L2/3 RS cells (n = 29) for large low (gray, 5%) and high (black, 80%) contrast stimuli. Bottom: plot of average PPC at individual gamma center frequency versus stimulus contrast for L2/3 RS units (n = 29, p < 0.0001 , Kruskal-Wallis ANOVA). **D:** Top: scatter plot of PPC values for single RS (black, n = 27, p = 0.0008, Wilcoxon signed rank test) and FS (green, n = 13, p = 0.003, Wilcoxon signed rank test) cells in response to full contrast cross (90˚ offset) and iso (0˚ offset) surround stimuli. Middle: average PPC spectra for L2/3 RS cells (n = 27) for full contrast cross (gray, 90˚ offset) and iso (black, 0˚ offset) surround stimuli. Bottom: plot of average PPC at individual gamma center frequency versus relative surround orientation for L2/3 RS units (n = 28, p = 0.004, Kruskal-Wallis ANOVA). Error bars in all plots represent s.e.m.; see Supp Fig 1 for FS data.

Behavioral state, often indexed by the locomotion of a head-fixed animal, can powerfully influence activity in the primary visual cortex (Niell & Stryker, 2010; Fu *et al.*, 2014; Pakan *et al.*, 2016) and the stimulus dependence of visual responses, specifically to contextual stimuli (Ayaz *et al.*, 2013; Dipoppa *et al.*, 2018). Therefore, we next asked if behavioral state influences stimulus-induced network synchronization. Although visual stimuli induced strong gamma oscillations in both running and non-running mice, we observed a substantial strengthening of gamma band power and spike-phase locking when mice were not locomoting (Fig. 3A-F). Importantly, locomotion suppressed gamma power and spike-phase coupling divisively across size, contrast, and relative center/surround orientation, largely preserving the feature dependence of gamma synchronization across these stimulus dimensions. Taken together, these data demonstrate that visually induced gamma band synchronization strongly depends on both the features of the visual stimulus and the animal's behavioral state. This allowed us to explore the underlying circuit mechanisms of this phenomenon by taking advantage of transgenic and optogenetic tools available in mice but not in higher mammalian species.

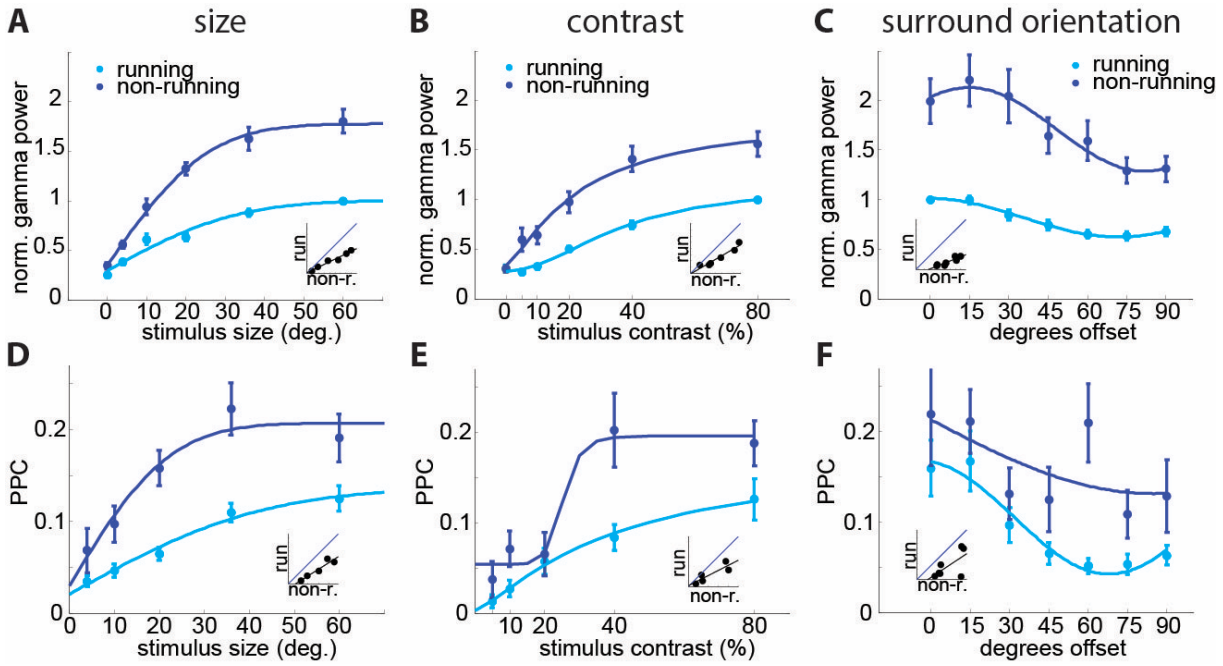

Figure 3: Gamma power and phase locking depend on behavioral state. A: Average normalized gamma power during running (light blue) and non-running (dark blue) versus stimulus size (n = 17, 2-way-ANOVA: main effect of size: $F(4,146) = 45.34$, $p<0.001$; main effect of running $F(1,146) = 122.49$, $p<0.001$; interaction: $F(4,146) = 6.40$, $p<0.001$). **B:** Average normalized gamma power during running and non-running versus stimulus contrast (n = 18, 2-way ANOVA: main effect of contrast: $F(4,149) = 33.68$, $p<0.001$; main effect of running: $F(1,149) = 67.82$, $p<0.001$; interaction: $F(4,149) = 1.39$, $p = 0.24$). **C:** Average normalized gamma power during running and non-running versus relative surround orientation (n = 10, 2-way ANOVA: main effect of oreintation: $F(6,108) = 6.38$, $p<0.001$; main effect of running: $F(1,108) = 156.02$, $p<0.001$; interaction: $F(6,108) = 1.34$, $p = 0.24$) **D:** Average PPC during running (light blue) and non-running (dark blue) versus stimulus size (n = 87, 2-way-ANOVA: main effect of size: $F(4,835) = 16.3$, $p<0.001$; main effect of running: $F(1,835) = 37.74$, $p<0.001$; interaction $F(4,835)$: 1.1, $p = 0.36$). **E:** Average PPC during running and non-running versus stimulus contrast (n = 29, 2-way-ANOVA: main effect of contrast: $F(4,256) = 14.02$, $p<0.001$; main effect of running: $F(1,256) = 13.49$, $p<0.001$; interaction: $F(4,256) = 1.9$, $p = 0.11$). **F:** Average PPC during running and non-running versus relative surround orientation (n = 28, 2-way-ANOVA: main effect of orientation: $F(6,328) = 3.75$, $p= 0.001$; main effect of running: $F(1,328) = 15.46$, $p<0.001$; interaction: $F(6,328) = 0.84$, $p = 0.54$). Error bars in all plots represent s.e.m.

VIP neurons control the gain of visually induced gamma oscillations in V1

Understanding the neural mechanisms that dynamically control gamma band entrainment may yield critical new insights into sensory computation and disease states. Therefore, we probed the cortical circuitry that might control the stimulus and state dependence of gamma band synchronization. Three features of gamma oscillations in V1 and the known connections of VIP neurons suggest that this interneuronal subclass may play a crucial role in regulating cortical synchronization in the gamma band. First, SST neurons, which are preferential postsynaptic targets of VIP neurons, are critical for visually induced gamma band oscillations in V1 (Veit *et al.*, 2017). Second, locomotion and brain state – which potently regulate gamma band power – are well known to powerfully modulate VIP neurons' activity (Lee *et al.*, 2013; Fu *et al.*, 2014; Jackson *et al.*, 2016). Third, gamma oscillations are known to be crucial for interareal coupling in the cortex (van Kerkoerle *et al.*, 2014; Bastos, Vezoli, Bosman, *et al.*, 2015; Bastos, Vezoli, & Fries, 2015), and VIP neurons are well-known targets of feedback axons from multiple higher cortical areas (Lee *et al.*, 2013; Zhang *et al.*, 2014; Wall *et al.*, 2016).

By the same token, three visual response properties of VIP neurons also potentially link them to gamma oscillations, as their activity is lowest when gamma is highest: VIP neurons are suppressed by high contrast, suppressed by large gratings, and suppressed by iso-oriented as compared to cross-oriented gratings (Keller, Dipoppa, *et al.*, 2020; Millman *et al.*, 2020; Mossing *et al.*, 2021). To directly probe these relationships we correlated gamma power to both average SST- and VIP-cell activity measured with two-photon imaging in a separate set of mice across size and contrast. While SST-cell activity was highest in conditions that also showed high gamma power (R: 0.76, p: 0.019), this relationship was opposite for VIP-cells (R: -0.84, p: 0.005). Gamma power is highest when VIP-cells are minimally active (Fig. 4). These strong correlations also held in the quiescent state (Fig 4 Suppl. 1, SST R: 0.93, p<0.001; VIP R: -0.73, p: 0.024).

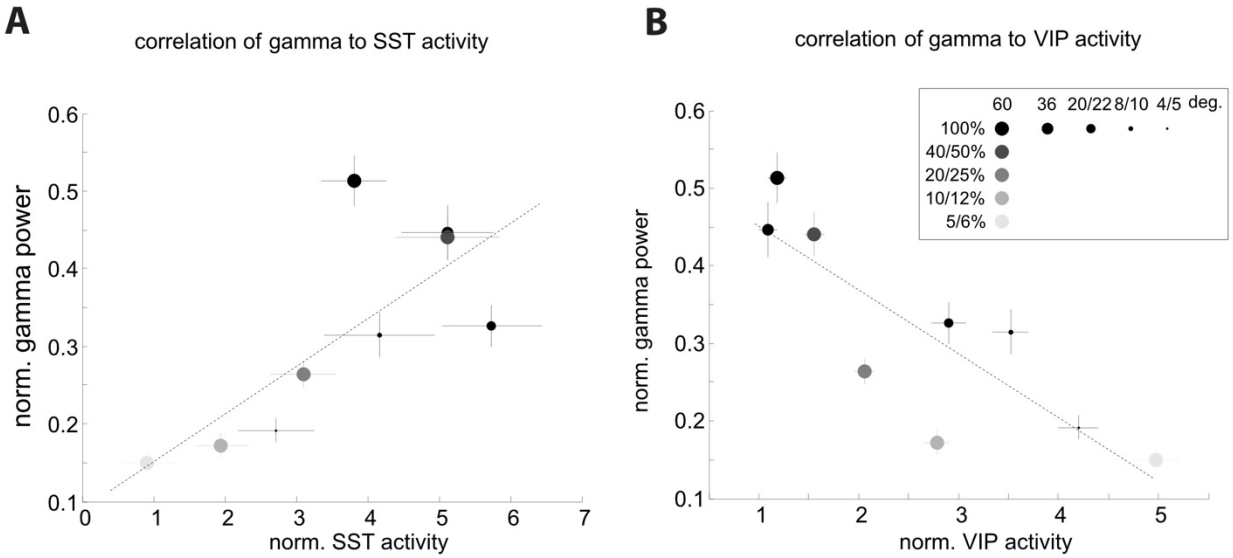

Figure 4: Opposing correlation of SST- and VIP-neuron activity with gamma power. A: Plot of averaged normalized gamma power in the running condition vs. averaged normalized SST-cell activity (deconvolved event-rate/mean), recorded via 2-photon imaging in a different set of animals across similar conditions. Different shades of gray represent different contrast levels and different symbol sizes represent different stimulus sizes. Dashed line is a linear fit of the data. SST-cell activity strongly correlates with gamma power (r(7) = 0.76, p = 0.019). **B:** Same as A, except for normalized VIP cell activity. VIP activity is strongly anti-correlated with gamma power (r(7) = -0.84, p = 0.005).

Due to the strong anti-correlation of VIP-cell activity and gamma power, we hypothesized that VIP neurons might actively desynchronize cortical ensembles. Moreover, they could crucially regulate the gain of gamma band synchronization, and help engender its feature selectivity and behavioral dependence. To test this hypothesis, we optogenetically suppressed VIP neurons in the same animals as described above via Cre-depdenent expression of the potent optogenetic silencer eNpHR3.0. Post-mortem histological analysis revealed widespread expression of eNpHR3.0 in superficial interneurons with bipolar morphology (Figure 5A). Illumination of the visual cortex in these mice resulted in significant and specific enhancements in narrowband gamma power across visual stimulus size, contrast, and center/surround orientation (Figure 5B-D). VIP neuron suppression multiplicatively enhanced gamma power across all feature dimensions, thereby scaling the gain of neural synchronization while preserving the overall shape of contrast, size and surround angle dependence (Fig. 5B-D bottom). In contrast, optogenetically suppressing VIP neurons had no effect on the higher frequency narrowband gamma oscillation derived from sub-cortical circuits, demonstrating a specific role of VIP in stimulus-induced cortically generated gamma synchronization only (Fig. 5 Suppl. 1).

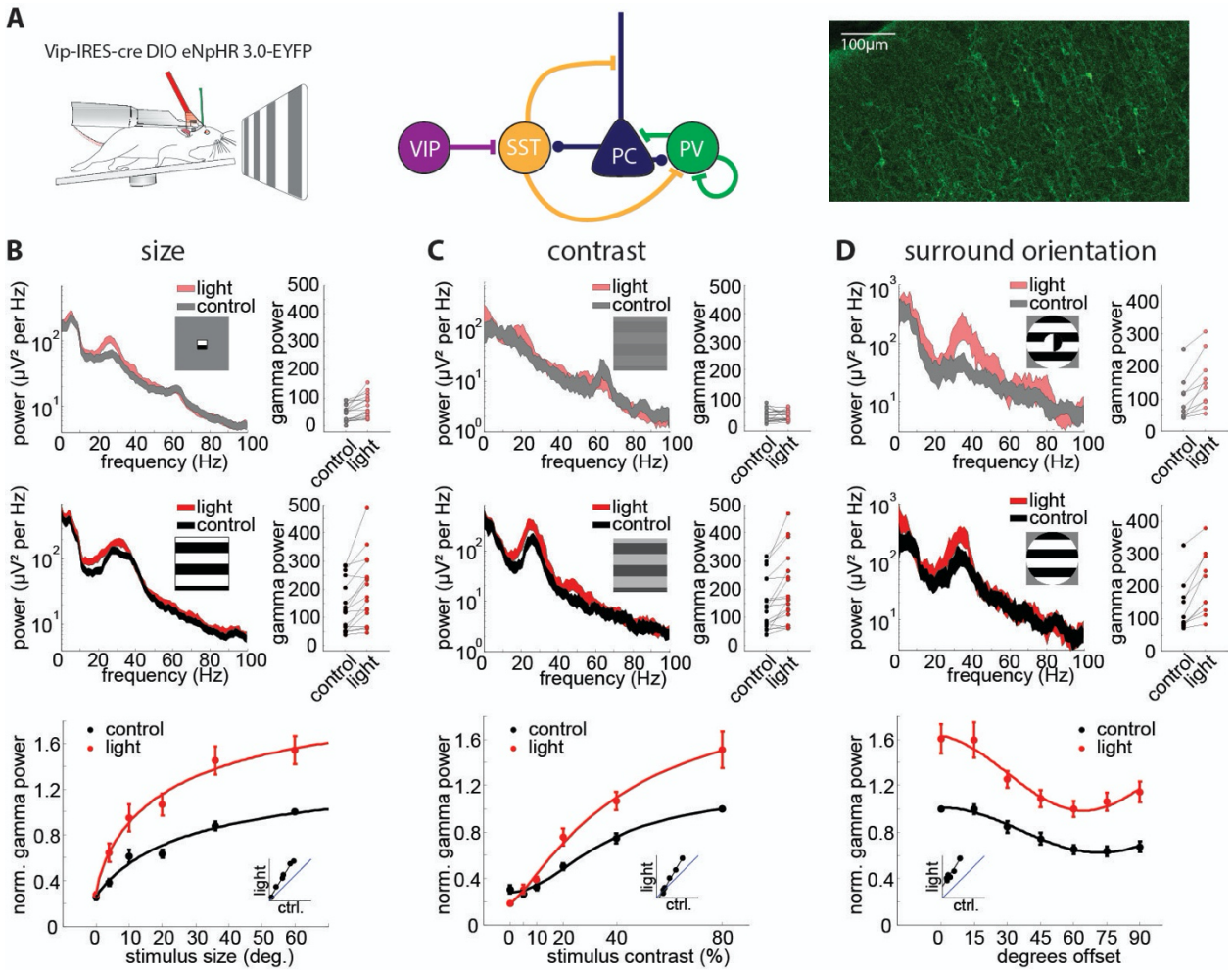

230 **Figure 5: VIP cells control the gain of visually induced gamma oscillations. A:** Left: Schematic of a head-fixed mouse on a running wheel with an optic fiber over the visual cortex and a laminar multi-electrode array in V1. Middle: Simplified circuit diagram with VIP cells disinhibiting PCs from SST inhibition. Right: Example image of a V1 brain section from a VIP-Cre mouse injected with a Cre-dependent AAV virus driving eNpHR3.0-YFP. **B:** Top: Left: example LFP power spectrum in response to a small (4˚) drifting grating with (red hue) and without (gray) light mediated suppression of VIP cells (thickness of line denotes mean ± standard error). Right: plot comparing the gamma power to small gratings with and without light (n = 17, p = 0.0003, Wilcoxon signed rank test). Middle: Left: example LFP power spectrum in response to a large (60˚) drifting grating with (red) and without (black) light mediated suppression of VIP cells (thickness of line denotes mean ± standard error). Right: plot comparing the gamma power to large gratings with and without light (n = 17, p = 0.0008, Wilcoxon signed rank test). Bottom: Average normalized gamma power with (red) and without (black) optogenetic suppression of VIP neurons versus stimulus size (n = 17, 2-way-ANOVA: main effect of light: F(1,160) = 54.18, p<0.001; main effect of size: F(4,160) = 22.18, p<0.001; interaction: F(4,160) = 1.03, p = 0.39). **C:** Top: Left: example LFP power spectrum in response to a low contrast (5%) drifting grating with (red hue) and without (gray) light-mediated suppression of VIP cells (thickness of line denotes mean ± standard error). Right: plot comparing the gamma power to low contrast gratings with and without light (n = 18, p = 0.45, Wilcoxon signed rank test). Middle: Left: example LFP power spectrum in response to a high contrast (80%) drifting grating with (red) and without (black) light-mediated suppression of VIP cells (thickness of line denotes mean ± standard error). Right: plot comparing the gamma power to high contrast gratings with and without light (n = 18, p = 0.0005, Wilcoxon signed rank test). Bottom: average normalized gamma power with (red) and without (black) optogenetic suppression of VIP neurons versus stimulus contrast (n = 18, 2-way-ANOVA: main effect of light: F(1,170) = 27.81, p<0.001; main effect of contrast: F(4,170) = 65.08, p<0.001; interaction: F(4,170) = 3.85, p = 0.005).**D:** Top: Left: example LFP power spectrum in response to a cross surround (90˚ offset) drifting grating with (red hue) and without (gray) light mediated suppression of VIP cells (thickness of line denotes mean ± standard error). Right: plot comparing the gamma power to cross surround gratings with and without light (n = 10, p = 0.002, Wilcoxon signed rank test). Middle: Left: example LFP power spectrum in response to an iso surround (0˚ offset) drifting grating with (red) and without (black) light mediated suppression of VIP cells (thickness of line denotes mean ± standard error). Right: plot comparing the gamma power to iso surround gratings with and without light (n = 10, p = 0.002, Wilcoxon signed rank test). Bottom: Average normalized gamma power with (red) and without (black) optogenetic suppression of VIP neurons versus relative surround orientation (n = 10, 2-way-ANOVA: main effect of light: F(1,125) = 119.37, p<0.001; main effect of orientation: F(6,125) = 13.14, p<0.001; interaction: F(6,125) = 0.88, p = 0.51).

Next, we asked if the enhancing effects of VIP neuron suppression on gamma power were also apparent in the synchronization of action potentials of individual neurons. Indeed, when suppressing VIP neurons, the great majority of recorded units showed substantial increases in phase-locking specifically to the network gamma rhythm (~30 Hz) (Example in Fig. 6A, and population curves in 6B-G, Fig. 6, Suppl. 1A-C). We found potent increases in phase locking across stimulus size, contrast, and relative center/surround orientation. The same was true for fast spiking, putative PV cells (Fig. 6, Suppl. 1D-F). These data demonstrate that VIP neurons potently control the gain of gamma band synchronization in mouse primary visual cortex, where their normal action is to constrain gamma band synchronization and decorrelate neural populations across three fundamental aspects of visual stimuli.

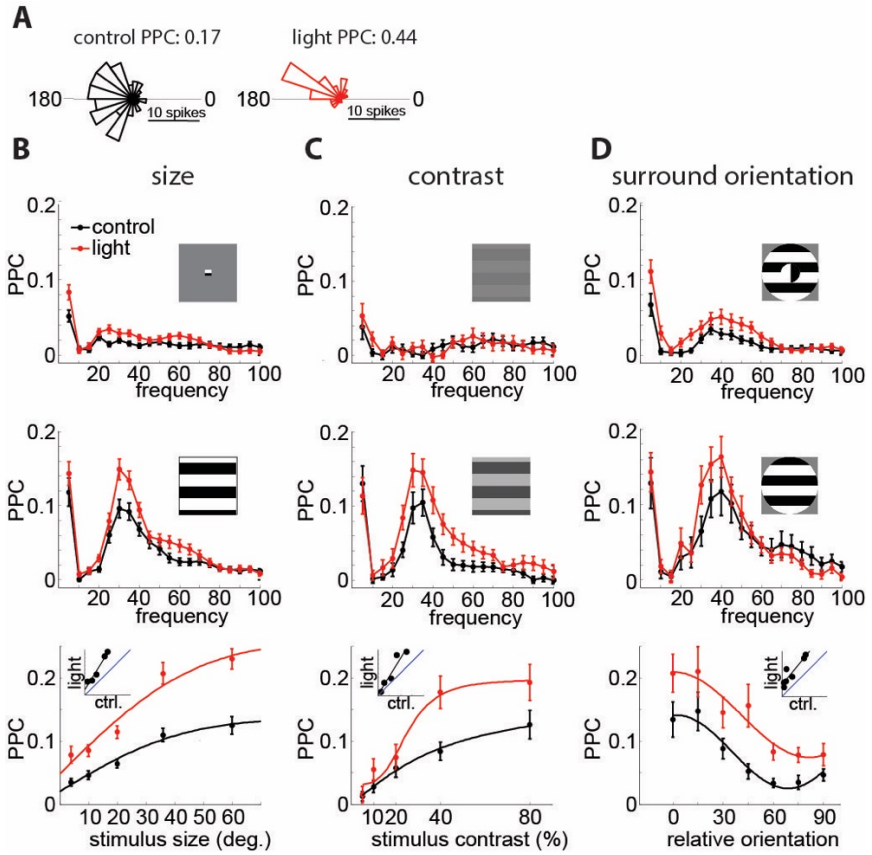

Figure 6: VIP cells control the strength of locking of single neurons to the visually induced gamma rhythm. A: Left: phase histogram of the spikes of an example L2/3 RS neuron relative to the gamma oscillation in the control condition (60˚ grating, same unit as in Fig. 2). Right: phase histogram of the spikes of the same neuron during inactivation of VIP neurons. **B:** Top: average PPC spectra for L2/3 RS cells with (red) and without (black) suppression of VIP cells (n = 78) for small (4˚) stimuli. Middle: average PPC spectra for L2/3 RS cells with (red) and without (black) suppression of VIP cells (n = 68) for large (60˚) stimuli. Bottom: Plot of average PPC versus stimulus size with (red) and without (black) light-mediated inactivation of VIP cells (n = 87, 2-way ANOVA: main effect of light: $F(1,857) = 78.42$, $p<0.001$; main effect of size: $F(4,857) = 42.83$, $p<0.001$; interaction: $F(4,857) = 3.14$, $p = 0.014$). **C:** Top: average PPC spectra for L2/3 RS cells with (red) and without (black) suppression of VIP cells (n = 27) for low contrast (5%) stimuli. Middle: average PPC spectra for L2/3 RS cells with (red) and without (black) suppression of VIP cells (n = 30) for high contrast (80%) stimuli. Bottom: Plot of average PPC versus stimulus contrast with (red) and without (black) inactivation of PV cells (n = 29, 2-way ANOVA: main effect of light: $F(1,280) = 13.01$, $p<0.001$; main effect of contrast: $F(4,280) = 21.8$, $p<0.001$; interaction: $F(4,280) = 2.17$, $p = 0.072$). **D:** Top: average PPC spectra for L2/3 RS cells with (red) and without (black) suppression of VIP cells (n = 46) for cross surround (90˚ offset) stimuli. Middle: average PPC spectra for L2/3 RS cells with (red) and without (black) suppression of VIP cells (n = 21) for iso surround (0˚ offset) stimuli. Bottom: Plot of average PPC versus relative surround orientation with (red) and without (black) inactivation of VIP neurons (n = 28, 2-way ANOVA: main effect of light: $F(1,378) = 28.66$, $p<0.001$; main effect of orientation: $F(6,378) = 10.31$, $p<0.001$; interaction: $F(6,378) = 0.69$, $p = 0.66$). Error bars in all plots represent s.e.m.

Since locomotion also potently regulates visually induced gamma oscillations (Fig. 3), we next probed whether VIP neurons contribute to the behavioral dependence of gamma band synchronization. We found that suppressing VIP neurons strongly enhanced gamma band power and phase coupling of V1 units across both locomoting and quiescent states (Fig. 7A-C), demonstrating that even during quiescence ongoing activity of VIP neurons is critical for controlling network synchronization (3-way ANOVA with factors light, locomotion and stimulus with post-hoc testing, all $p<0.001$, no interactions). To test whether the magnitude of the behavioral-state modulation of gamma oscillations was altered by VIP neuron suppression, we computed a 'behavioral modulation index' (BMI, (quiescence-locomotion)/(quiescence+locomotion)) that represents the normalized change in gamma power between locomotion and quiescence. During optogenetic suppression of VIP neurons, we found a significant reduction in BMI across size and surround angle stimulus conditions (Fig. 7D-F), demonstrating that VIP neurons regulate the behavioral modulation of network synchronization in mouse V1, if a visual stimulus is strong enough. Across the different contrast levels the reduction of BMI was only significant for the highest contrast level (80%).

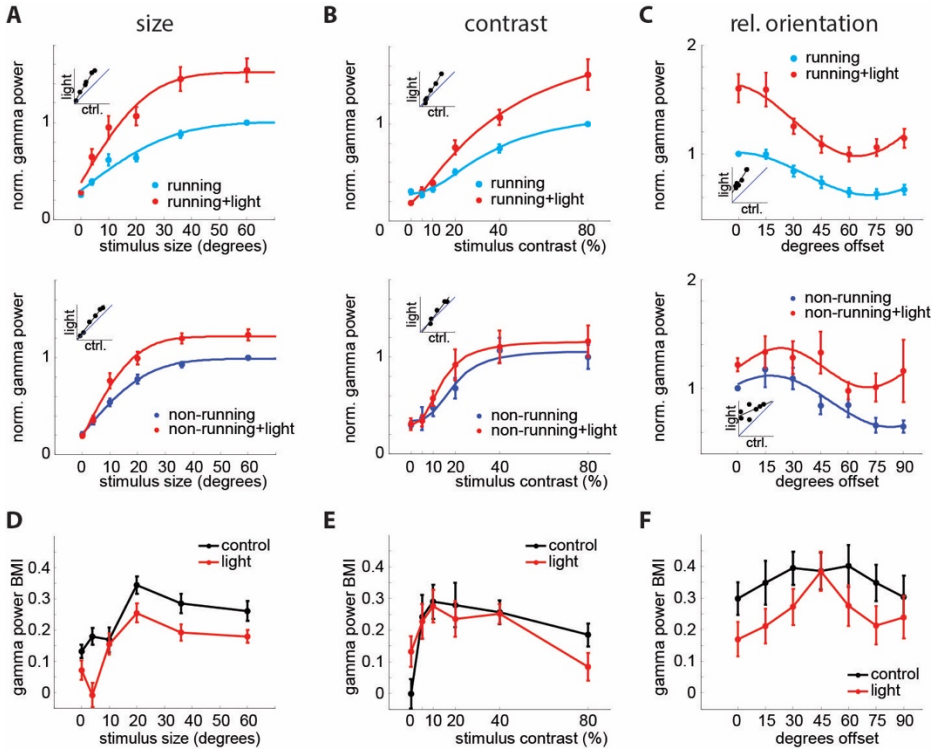

Figure 7: VIP neurons contribute to the behavioral dependence of gamma band synchronization. A: Top: Average normalized gamma power as a function of stimulus size with (red) and without optogenetic suppression of VIP neurons during running (light blue, n = 21, 2-way ANOVA: mian effect of light: $F(1,160) = 54.18$, $p<0.001$; main effect of size: $F(4,160) = 22.18$, $p<0.001$; interaction: $F(4,160) = 1.03$, $p = 0.39$) Bottom: Same for non-running (dark blue, n = 21, 2-way-ANOVA: main effect of light: $F(1,130) = 26.49$, $p<0.001$; main effect of size: $F(4,130) = 55.9$, $p<0.001$; interaction: $F(4,130) = 1.41$, $p = 0.23$). **B:** Top: Average normalized gamma power as a function of stimulus contrast with (red) and without optogenetic suppression of VIP neurons during running (light blue, n = 21, 2-way ANOVA: main effect of light: $F(1,170) = 27.81$, $p<0.001$; main effect of contrast: $F(4,170) = 65.08$, $p<0.001$; interaction: $F(4,170) = 3.85$, $p = 0.005$) Bottom: Same for non-running (dark blue, n = 21, 2-way-ANOVA: main effect of light: $F(1,125) = 1.48$, $p = 0.23$; main effect of contrast: $F(4,125) = 12.36$, $p<0.001$; interaction: $F(4,125) = 0.31$, $p = 0.87$). **C:** Top: Average normalized gamma power as a function of relative surround angle with (red) and without optogenetic suppression of VIP neurons during running (light blue, n = 10, 2-way ANOVA: main effect of light: $F(1,125) = 119.37$, $p<0.001$; main effect of orientation: $F(6,125) = 13.14$, $p<0.001$; interaction: $F(6,125) = 0.88$, $p = 0.51$) Bottom: Same for non-running

(dark blue, n = 7, 2-way-ANOVA: main effect of light: $F(1,83) = 11.27$, $p= 0.001$; main effect of orientation: $F(6,83) = 1.9$, $p = 0.09$; interaction: $F(6,83) = 0.47$, $p = 0.83$). **D:** Average gamma power BMI (behavioral modulation index) as a function of stimulus size with (red) and without (black) optogenetic suppression of VIP neurons (n = 21, 2-way-ANOVA: main effect of light: $F(1,134) = 14.34$, $p<0.001$; main effect of size: $F(4,134) = 8.84$, $p<0.001$; interaction: $F(4,134) = 1.29$, $p = 0.28$). **E:** Average gamma power BMI as a function of stimulus contrast with (red) and without (black) optogenetic suppression of VIP neurons (n = 21, 2-way-ANOVA: main effect of light: $F(1,130) = 0.66$, $p = 0.42$; main effect of contrast: $F(4,130) = 1.79$, $p = 0.14$; interaction: $F(4,130) = 0.22$, $p = 0.93$). **F:** Average gamma power BMI as a function of relative surround angle with (red) and without (black) optogenetic suppression of VIP neurons (n = 10, 2-way-ANOVA: main effect of light: $F(1,92) = 7.44$, $p = 0.008$; main effect of orientation: $F(6,92) = 1.03$, $p = 0.41$; interaction: $F(6,92)$, $p = 0.96$).

VIP neurons decouple V1 ensembles that process non-matched visual features

One of the most striking features of V1 gamma band oscillations is that they preferentially synchronize distant neurons that are processing parts of a large stimulus with homogeneous statistics, such as a common orientation and direction of motion (Gray *et al.*, 1989), indicative of belonging to a common object. Although long-range excitatory axons are likely to be essential for this coupling across the retinotopic map, we speculated that VIP neurons, which suppress gamma synchronization, could actively decouple distributed ensembles that are processing non-matched features, thus preventing promiscuous synchrony. To test this, we place one multielectrode array in the retinotopic region corresponding to the center of the grating, and one in a distal region representing the surround (Fig. 8A, average electrode separation: 530+-90 μm n = 7, 15±3 visual degrees n = 11, Fig. 8 Suppl. 1). Similar to findings in cats (Gray *et al.*, 1989), large, homogeneous ('iso-oriented') drifting gratings drove highly coherent LFP gamma oscillations between the two separate sites (Fig. 8B). However, when the grating orientation for the two separated electrode arrays was orthogonal ('cross-oriented'), coherence, specifically in the gamma band, dropped substantially (Fig. 8B 23+-5.7%, p = 0.004 Wilcoxon signed rank). Next, we tested the hypothesis that VIP neurons might contribute to this differential locking across visual space by preferentially suppressing coherence for cross-oriented gratings. Indeed, optogenetically suppressing VIP neurons had no impact on coherence for iso-oriented gratings (Fig. 8C,D, 4.5+-2.6%, p = 0.16, Wilcoxon signed rank test), but significantly increased coherence for cross-oriented gratings (18.6+-8.2%, p = 0.008, Wilcoxon signed rank test). The impact on coherence for cross-oriented gratings was highly specific to the visually induced gamma band (~30 Hz) (Fig. 8E,F). Compared across all different offset angles there was a trend of suppressing VIP activity to detune the function between coherence and center/surround orientation (Figure 8G). This demonstrates that VIP neuron activity critically contributes to long-range synchronization of primary visual cortical ensembles: they preferentially suppress synchrony when the stimulus features for distant ensembles do not match. Importantly, even though VIP neuron suppression profoundly enhanced local gamma power in response to iso-oriented gratings (see Fig. 5D), it did not significantly increase coherence. This implies that long range coherence beween spatially separated assemblies is not a necessary consequence stronger local gamma band activity, but regulated by distinct mechanism, potentially involving VIP neurons. Note that the lack of an increase in coherence for iso-oriented stimuli was not due to a ceiling effect, as the measured coherence was substantially less than the theoretical maximum of 1 (mean coherence iso: 0.60+/-0.04, mean coherence iso+light: 0.62+/-0.04 iso)(Fig. 8C).

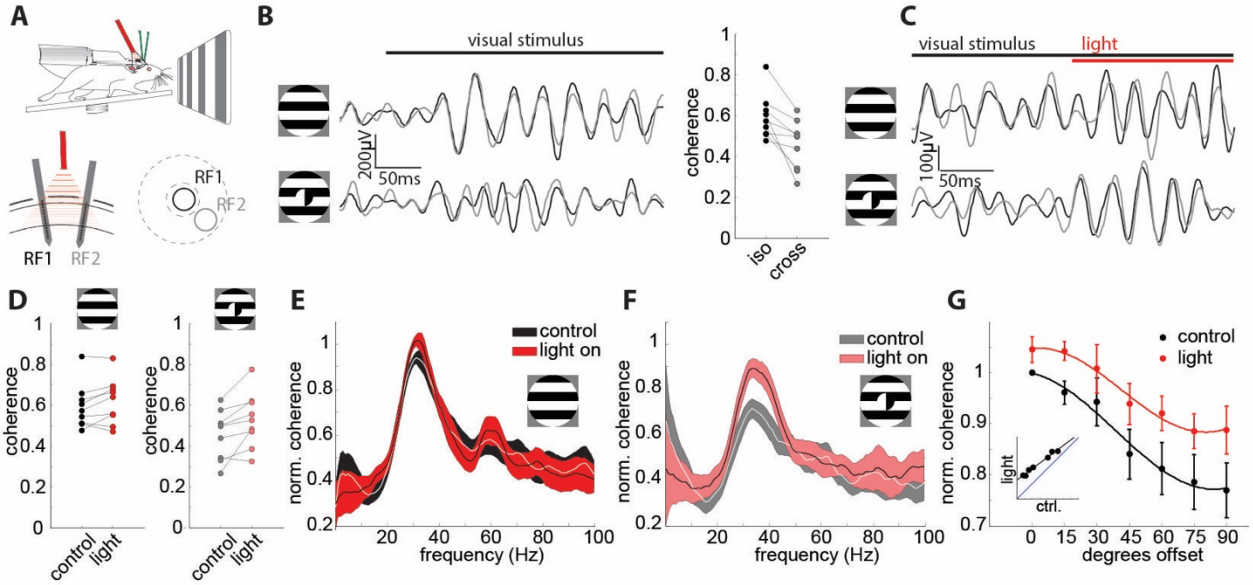

Figure 8: VIP neurons decouple V1 ensembles that process non-matched visual features A: Top: recording schematic with two independent laminar probes in V1 of awake, head-fixed VIP-Cre mice. Bottom left: Schematic of the multielectrode array recording configuration with two laminar arrays in distant sites (530+-90 µm apart, histology from n = 7 mice) recorded from two separate receptive fields (RF1 and RF2, 15° ± 3° of visual angle separation, n = 11 mice). Bottom right: schematic of the receptive fields' locations on the two laminar probes. The center and surround of the gratings are indicated with dashed lines. **B:** Left: Example filtered LFP traces in response to an iso (0˚ offset, top) and a cross (90˚ offset, bottom) oriented surround relative to the center. Traces from the center recording site are plotted in black, traces from the surround in gray. Right: Plot comparing the LFP gamma band coherence for iso-oriented to cross-oriented surround stimuli (n = 9, p = 0.004, Wilcoxon signed rank test). **C:** Example filtered LFP traces in response to an iso (0˚ offset, top) and a cross (90˚ offset, bottom) oriented surround relative to the center. Traces from the center recording site are plotted in black, traces from the surround in gray. The onset of light to suppress VIP cell activity is shown as a red bar on top. **D:** Left: Plot comparing the LFP gamma band coherence for iso-oriented surround stimuli for control (black) and VIP inactivation (red) trials (n = 9, p = 0.16, Wilcoxon signed rank test) Right: Plot comparing the LFP gamma band coherence for cross-oriented surround stimuli for control (gray) and light (light red) trials (n = 9, p = 0.008, Wilcoxon signed rank test). **E:** Population averaged normalized coherence spectra for iso-oriented surround stimuli for control (black) and light (red) trials (n = 10, thickness of line denotes mean ± standard error). **F:** Population averaged coherence spectra for cross-surround stimuli for control (gray) and light (light red) trilas (n = 10, thickness of line denotes mean ± standard error). **G:** Plot of average normalized coherence versus relative surround orientation with (red) and without (black) inactivation of VIP neurons (n = 9, 2-way ANOVA: main effect of light: F(1,107) = 18.8, p<0.001; main effect of offset angle: F(6,107) = 9.16, p<0.001; interaction: F(6,107) = 0.22, p = 0.97). Error bars represent s.e.m.

Discussion

Neural synchronization, particularly in the gamma band, is observed widely throughout neural systems, from insects to humans (Lutzenberger *et al.*, 1995; Tallon *et al.*, 1995; Wehr & Laurent, 1996). Synchronization on millisecond timescales has been postulated to play diverse roles in brain function, including perceptual binding, inter-areal communication, attention, and motor planning (Fries, 2009). Ample evidence from humans has linked impaired gamma oscillations to neurological disorders, including schizophrenia (Uhlhaas & Singer, 2010; Mathalon & Sohal, 2015). Post-mortem analysis has even revealed changes in the inhibitory neuron subtypes in some of these patients (Lewis *et al.*, 2012), raising the idea that the selective degeneration or malfunction of inhibitory neurons subtypes may contribute to the etiology of these diseases. The data in this study establish a third class of cortical interneuron – the disinhibitory VIP cell, as a crucial regulator of gamma rhythms in the primary visual cortex.

Despite ample research, the function of gamma rhythms remains somewhat controversial (Chalk *et al.*, 2010; Ray & Maunsell, 2010, 2015; Sedley & Cunningham, 2013; Brunet *et al.*, 2014;

Hermes *et al.*, 2015), partially owing to a lack of more specific tools to manipulate them in the context of perception and behavior. Although multiple mechanisms can drive synchronization, in many areas local synaptic inhibition is responsible for generating gamma rhythms and phase locking neurons (Bartos *et al.*, 2007; Buzsáki & Wang, 2012). In the sensory cortex of mice, recent studies have established a key role for PV and SST neurons in different types of cortical rhythms (Cardin *et al.*, 2009; Sohal *et al.*, 2009; Siegle *et al.*, 2014; Chen *et al.*, 2017; Veit *et al.*, 2017; Hakim *et al.*, 2018). SST neurons are responsible, more specifically, for visually induced, context-dependent oscillations in the 20-40 Hz frequency band (Chen *et al.*, 2017; Veit *et al.*, 2017) that are the focus of this study. Note that while Chen et. al. call the visually induced rhythm 'beta' as its peak frequency often lies below 30 Hz, it shares key features with visually induced gamma rhythms in primates and cats, including its contrast, size and center/surround orientation dependence (Gray *et al.*, 1989; Gieselmann & Thiele, 2008; Ray *et al.*, 2013). For this reason we call it 'gamma' here as in our prior study. As we show here, the magnitude of these gamma rhythms, and the strength of the phase locking of the local neurons, depends strongly on multiple key features of the visual stimulus. Gamma power increases monotonically with stimulus contrast and size, but decrements when the center and surround of the grating have increasingly different orientations. This feature dependence largely agrees with prior studies in cats and primates (Gray *et al.*, 1989; Gieselmann & Thiele, 2008; Ray & Maunsell, 2011; Ray *et al.*, 2013; Murty *et al.*, 2018), implying that the underlying mechanisms of these oscillations might be conserved across mammalian species. Since gamma power depends heavily on the statistical structure of the stimulus content beyond the classical receptive fields of V1 neurons, they might specifically contribute to computational processes related to the encoding of global stimulus properties, and facilitate figure/ground segregation and object identification in downstream visual cortical areas (van Kerkoerle *et al.*, 2014; Self *et al.*, 2016).

This study shows that VIP neurons have at least three key functions in the control of visually induced gamma rhythms in V1. First, they regulate the gain of gamma band synchronization, for stimulus contrast and size, and for the relative orientation of the center and surround of a grating. Likely by directly suppressing SST neuron activity, they prevent the hyper-synchronization of cortical pyramidal neurons which could lead to the aberrant propagation of activity within or across visual areas or erroneous perceptual binding. In the same vein, VIP neuron activity might enhance visual perception by expanding the dynamic range of stimulus-dependent oscillatory dynamics. Second, VIP neurons regulate gamma band synchrony across behavioral state (quiescence vs. locomotion) and contribute to the state-dependent gain of neural synchronization by preferentially decorrelating V1 networks during locomotion. Third, and perhaps most importantly, VIP neurons critically contribute to the differential coupling of distal V1 ensembles processing matched versus non-matched global stimulus properties, preferentially suppressing synchronization when the stimulus features driving the two ensembles conflict. Through these three actions VIP neurons might enhance the encoding of contextual visual stimuli, promote the effective propagation of neural activity within and between cortical areas, and potentially contribute to the perceptual binding of disparate features of a visual stimulus.

A key outstanding question is what excitatory inputs drive VIP neurons, and in turn, how they mediate their feature-specific effects on gamma rhythm gain and phase locking. VIP neurons are well-known targets of cholinergic afferents from the basal forebrain, which likely contributes to their enhanced activity during alertness and locomotion (Fu *et al.*, 2014). This cholinergic input could also explain their putative role in learning (Letzkus *et al.*, 2011), as well as the increased impact of VIP neuron activity on gamma rhythms in active behavioral states. VIP neurons can also co-release acetylcholine (Eckenstein & Baughman, 1984; Dudai *et al.*, 2020; Granger *et al.*, 2020) and neuropeptides, which may play a role, since acetylcholine modulates gamma power both in cortical and subcortical structures (Bhattacharyya *et al.*, 2013; Bryant *et al.*, 2015). VIP neurons are also known targets of corticocortical feedback axons from higher cortical areas,

including motor cortex, cingulate cortex, and higher visual areas (Lee *et al.*, 2013; Zhang *et al.*, 2014). This input might be crucial for their context-specific effects, as neurons in higher visual and more frontal areas are known to effectively encode global stimulus properties and spatial context. Finally, VIP neurons are also local targets of V1 horizontal axons in layer 2/3, and are therefore well integrated into the local network (Xu & Callaway, 2009; Karnani, Jackson, Ayzenshtat, Tucciarone, *et al.*, 2016). Thus, they may receive rhythmic excitatory input from pyramidal cells and rhythmic inhibition from SST neurons. The next question is how VIP neurons exert their effects on gamma entrainment of the rest of the V1 network. Their strong and preferential innervation of SST neurons (Pfeffer *et al.*, 2013), which are critical for the visually induced gamma rhythm, is one plausible explanation. By suppressing SST neurons and thus reducing their inhibitory action on pyramidal and PV neurons, VIP neurons should be able to dynamically control the strength of gamma synchronization. The fact that VIP activity so potently alters gamma oscillations in V1 lends additional support to the notion that SST-mediated inhibition is crucial for visually induced synchronization in V1. This relationship might also explain why we see little effect on the BMI in the case of contrast modulation. Only if SST cells were sufficiently driven by visual inputs, would their disinhibition through VIP inactivation become observable in the network. Thus, low contrast sensitivity of SST cells (Millman *et al.*, 2020; Mossing *et al.*, 2021) could be the reason for the lack of an effect on BMI for low contrast conditions.

Our data reveal a key new mechanism for the dynamic control of gamma-band neural synchronization in the primary visual cortex. As the same disinhibitory circuits exist in other sensory and higher cortical areas, the role of VIP neurons in controlling the gain and specificity of gamma entrainment might be a general feature of cortical networks. Furthermore, our data suggest that VIP neurons might be potential therapeutic targets in neurological disorders that are associated with altered gamma rhythms and defects in inhibitory neural circuitry. Optogenetic or pharmacological tools aimed at re-balancing activity in VIP neurons, or perhaps more specific subsets of VIP neurons, should thus be useful in understanding the role of gamma rhythms in normal brain function and perhaps correcting it in disease.

Methods

Transgenic mice

All experiments were performed in accordance with the guidelines and regulations of the ACUC of the University of California, Berkeley. Mice for the *in vivo* experiments were housed in groups of five or less with a 12:12h light:dark cycle. Both female and male mice were used. Experiments *in vivo* were performed on animals aged between 8–27 weeks during their subjective night. We used VIP-IRES-Cre (JAX stock 010908) mice. Mice were out-crossed for one generation to the ICR white strain (Charles River).

Viral infection

Neonatal VIP-Cre mice (P3–6) were briefly cryo-anesthetized and placed in a head mold. Transcranial injection of ~45nl of undiluted AAV9-EF1a-DIO-eNpHR3.0-YFP (22 animals) was performed using a Drummond Nanoject injector at three locations in V1 using a glass pipette beveled to fine tip (~30-60μm). With respect to the lambda suture coordinates for V1 were 0.0 mm AP, 2.2 mm L and injection was as superficial as possible under the skull.

Preparation for in vivo *recording*

Mice were anesthetized with isoflurane (2.5% vapor concentration). The scalp was removed, the fascia retracted, and the skull lightly etched with a 27 gauge needle. Following application of Vetbond to the skull surface, a custom stainless steel headplate was fixed to the skull with dental cement (Metabond). Mice were allowed to recover from surgery for at least 2 days. Then mice were habituated for 2–10 days to head-fixation on a free-spinning circular treadmill. On the day of recording mice were briefly anesthetized with isoflurane (2%), the skull over V1 was thinned, and one or two (spacing 400-1000μm) small (<250 μm) craniotomies were opened over V1 with a fine needle.

Visual stimulation

Visual stimuli were generated with Psychophysics Toolbox (Brainard, 1997) running on an Apple Mac Mini and were presented on a gamma corrected 23-inch Eizo FORIS FS2333 LCD display with a 60-Hz refresh rate. At the beginning of each recording session the receptive fields of MUA recorded at each cortical location was mapped with sparse noise to be able to precisely position the grating stimuli. The stimulus was centered on a location where a small grating, movable by hand, elicited a clear response. Sparse noise consisted of black and white squares (2 visual degrees, 80 ms) on a 20x20 visual degree grid flashed onto a gray background of intermediate luminance. To improve receptive field estimation the same stimulus grid was offset by 1 degree and the resulting maps were averaged. MUA average receptive fields were calculated by reverse correlation.

Visual stimuli consisted of drifting square-wave gratings at 0.04 cycles per degree and 2 cycles per second centered on the average MUA receptive field presented for 2s with at least 1s inter stimulus interval. Gratings were presented in three different configurations: 1) full contrast gratings of eight different directions (0–315° in steps of 45°) and five different sizes (4 10, 20, 36, and, if possible, 60 visual degrees – if the RF was not perfectly centered on the monitor, the effective largest size was slightly smaller); 2) gratings of four different directions (0-270° in steps of 90°), three different sizes (8,20 and 60°) and 5 different contrast levels (0.05, 0.1, 0.2, 0.4, 0.8) Michelson contrast and 3) full contrast square-wave gratings with a circular aperture of 8-15° visual degrees diameter (depending on the separation of the two RFs), centered on the MUA receptive field of one of the two simultaneously recorded cortical locations, that was surrounded by a 60 degree grating with one of seven different relative orientations (0-180° in steps of 30°). For the coherence analysis we only analyzed cases in which the second receptive field was covered entirely and exclusively by the surround-stimulus (see Fig. 7A and sup. Fig. 2).

Optogenetic stimulation in vivo

For optogenetic stimulation of eNpHR3.0 in vivo we used red (center wavelength: 625 nm) from the end of a 1-mm diameter multimode optical fiber coupled to a fiber coupled LED (Thorlabs) controlled by digital outputs (NI PCIe-6353). The fiber was placed as close to the craniotomy as possible (<3 mm). The illumination area was set to illuminate a wide area including all of V1. Light levels were tested in increasing intensities at the beginning of the experiment and were kept at the lowest possible level that still evoked observable change in ongoing activity for the remainder of the recording. We only used viral injections into V1, and did not attempt to use an eNphR transgenic reporter line to avoid off-target expression of the opsin and non-specific optogenetic suppression of subcortical nuclei (such as the thalamic reticular nucleus).

Gratings drifted for 2s with at least 1s inter-trial intervals with the red LED switched on for 1 s starting 0.5 s after start of the visual stimulus in 50% of the trials. The period of light was chosen to influence the stable steady-state of the response to the grating and all analysis was performed during this time window.

In vivo extracellular multi-electrode electrophysiology

One or two 16-channel linear electrodes with 25 micron spacing (NeuroNexus, A1x16-5mm-25-177-A16) were guided into the brain using micromanipulators (Sensapex) and a stereomicroscope (Leica). Electrical activity was amplified and digitized at 30 kHz (Spike Gadgets), and stored on a computer hard drive. The cortical depth of each electrical contact was determined by zeroing the bottom contact to the surface of the brain. Electrodes were inserted close to perpendicular to the brain's surface for single electrode recordings and ~25 degrees from vertical for the two electrode experiments. After each recording a laminar probe coated with the lipophilic dye DiI was used to mark each electrode track to quantitatively assess insertion angle and depth with post-hoc histologic reconstructions. The laminar depth of recorded units was corrected for the insertion angle and the local curvature of the neocortex.

Analysis of local field potential data

All analysis was performed using custom written code or openly available packages in Matlab (Mathworks). Local field potentials were extracted by low pass filtering the raw signal, sampled at 30 kHz, below 200 Hz and subsequent down-sampling to 1 kHz. For LFP-only analysis we always analyzed the LFP from the electrode contact closest to a cortical depth of ~350 μm (in cortical layer 3). For spike locking to the LFP we used the LFP from an electrode contact 50 μm away from the contact with the largest spike-waveform amplitude to reduce contamination of the LFP.

The power spectrum was computed in a 800 ms analysis window starting 200 ms after light onset (to exclude any photo-electric artifacts sometimes present in the first ~150 ms after light onset) using multi-taper estimation in Matlab with the Chronux package (http://chronux.org/, Mitra & Bokil, 2007) using 3 tapers. All power analysis was performed on the power at the peak of each animal's specific gamma oscillation in the specific visual stimulation condition. Peaks were identified as local maxima on the smoothed spectrum between 20 and 40Hz that were preceded by local minima in the 15Hz preceding the peak. If no true peak could be found (as was often the case for very small or low contrast conditions), we took the power at the frequency of the peak for the highest contrast/largest stimulus of that animal.

For calculation of coherence, bipolar derivatives of the LFP were calculated by subtracting the electrode channel two contacts above the channel of interest (50μm distance), to remove the common recording reference and to enhance spatial specificity of the signal. Coherence between the two recording sites was determined using the chronux package with the same number of tapers as the power analysis. All spectral plots show mean±s.e.m, the coherence spectra show jack-knifed 95% confidence intervals. Coherence values for the analysis were taken of the peak of each animals' individual coherence spectrum as for the power above.

Analysis of spiking data

Spiking activity was extracted by filtering the raw signal between 800 and 7000 Hz. Spike detection was performed using the UltraMega Sort package (Hill et al., 2011). Detected spike waveforms were sorted using the MClust package (http://redishlab.neuroscience.umn.edu/MClust/MClust.html). Waveforms were first clustered automatically using KlustaKwik and then manually corrected to meet criteria for further analysis. With the exception of <25 burst firing units, included units had no more than 1.5% of their individual waveforms violating a refractory period of 2 ms. Individual units were classified as either fast-spiking or regular spiking using a k-means cluster analysis of spike waveform components. Since the best separation criterion was the trough-to-peak latency of the large

negative going deflection and clustering is non-deterministic, we defined all units with latencies shorter than 0.36 ms as fast spiking and all units with latencies larger than 0.38ms as regular spiking. Cells with intermediate latencies were excluded from further analysis.

The depth of each unit was assigned based on the calculated depth of the electrode on the array that exhibited its largest amplitude sorted waveform. Layer boundaries were determined following a previously established approach (Pluta *et al.*, 2015). Firing rates were computed from counting spikes in a 1 second window starting 500 ms after the onset of the visual stimulus, which coincided with the onset of the LED during optogenetic suppression trials. Unless otherwise stated, we only analyzed trials when the animal was moving (at least 1cm/s) and not accelerating or decelerating abruptly (not more than 1.5 s.d. deviation from the animal's mean running speed).

To quantify locking of spiking activity to the gamma band we bandpass filtered the LFP in a 20 Hz band around the individual gamma band peak (between 20 and 45 Hz) and extracted the oscillation's instantaneous phase by using the imaginary part of the analytical signal using the Hilbert transform. Each spike is thus assigned an exact phase in the gamma oscillation. Phase locking magnitude is determined for each unit by the pairwise phase consistency (PPC), a measure of synchrony that is not biased by the number of spikes (Vinck *et al.*, 2010). We only included units that fired more than 20 spikes total in response to the largest grating size in the control condition and whose average visual response rate was >1Hz. PPC-spectra were calculated as above but for LFP filtered into 20 non-overlapping 5Hz wide frequency bands.

Behavioral modulation index (BMI) was calculated as $(R_r - R_s)/(R_r + R_s)$ where R_r is the average response during running and R_s is the average response in non-running (still) trials.

For illustrative purposes the average functions for gamma power and PPC were fit with functions. For size tuning curves an integral of Gaussian, for contrast tuning a Naka-Rushton function and for center-surround angle a sinusoid was fit with Matlab curve fitting toolbox.

Imaging data

Imaging data was performed as described in (Mossing *et al.*, 2021). Briefly, Sst-IRES-Cre and Vip-IRES-Cre mice wer crossed to Ai162(TIT2L-GC6s-ICL-tTA2)-D mice (RRID:IMSR_JAX:031562) and an imaging window implanted. The visual stimulus consisted of square wave drifting gratings, with directions tiling 0-360 degrees at 45° intervals, with a spatial frequency of 0.08 cycles per degree, and a temporal frequency of 1 Hz. Visual stimulus presentation lasted one second,followed by a one second inter-stimulus interval. Mice were head-fixed on a freely spinning running wheel under a Nixon 16x-magnification water immersion objective and imaged with a two-photon resonant scanning microscope (Neurolabware) within a light tight box. The imaging FOV was 430 by 670 um, with four planes spaced 37.5 µm apart imaged sequentiallyusing an electrotunable lens (Optotune), sampling each plane at an effective frame rate of 7.72 Hz. Motion correction and ROI segmentation was performed using Suite2p (Pachitariu *et al.*, 2017). Neuropil subtraction was applied as described in (Pluta *et al.*, 2017). ΔF/F traces were calculated as $\frac{\Delta F}{F} = \frac{F(t)-F_0}{F_0}$ with baseline F_0 computed over a sliding 20th percentile filter of width 3000 frames. Because the inter-stimulus interval was short to permit more stimuli to be displayed, calcium transients overlapped between successive trials. Therefore, we deconvolved calcium traces for this data using OASIS with L1 sparsity penalty (Friedrich *et al.*, 2017) using ΔF/F traces as input. We report this deconvolved event rate normalized by the mean.

References

Adesnik, H., Bruns, W., Taniguchi, H., Huang, Z.J., & Scanziani, M. (2012) A neural circuit for spatial summation in visual cortex. *Nature*, **490**, 226–231.

Adrian, E.D. (1950) The electrical activity of the mammalian olfactory bulb. *Electroencephalogr Clin Neurophysiol*, **2**, 377–388.

Askew, C.E., Lopez, A.J., Wood, M.A., & Metherate, R. (2019) Nicotine excites VIP interneurons to disinhibit pyramidal neurons in auditory cortex. *Synapse*, **73**, e22116.

Ayaz, A., Saleem, A.B., Schölvinck, M.L., & Carandini, M. (2013) Locomotion Controls Spatial Integration in Mouse Visual Cortex. *Current Biology*, **23**, 890–894.

Ayzenshtat, I., Karnani, M.M., Jackson, J., & Yuste, R. (2016) Cortical Control of Spatial Resolution by VIP+ Interneurons. *J Neurosci*, **36**, 11498–11509.

Bartoli, E., Bosking, W., Chen, Y., Li, Y., Sheth, S.A., Beauchamp, M.S., Yoshor, D., & Foster, B.L. (2019) Functionally Distinct Gamma Range Activity Revealed by Stimulus Tuning in Human Visual Cortex. *Curr Biol*, **29**, 3345-3358.e7.

Bartos, M., Vida, I., Frotscher, M., Meyer, A., Monyer, H., Geiger, J.R.P., & Jonas, P. (2002) Fast synaptic inhibition promotes synchronized gamma oscillations in hippocampal interneuron networks. *Proc Natl Acad Sci U S A*, **99**, 13222–13227.

Bartos, M., Vida, I., & Jonas, P. (2007) Synaptic mechanisms of synchronized gamma oscillations in inhibitory interneuron networks. *Nature Reviews Neuroscience*, **8**, 45–56.

Bastos, A.M., Vezoli, J., Bosman, C.A., Schoffelen, J.-M., Oostenveld, R., Dowdall, J.R., De Weerd, P., Kennedy, H., & Fries, P. (2015) Visual Areas Exert Feedforward and Feedback Influences through Distinct Frequency Channels. *Neuron*, **85**, 390–401.

Bastos, A.M., Vezoli, J., & Fries, P. (2015) Communication through coherence with inter-areal delays. *Current Opinion in Neurobiology*, **31**, 173–180.

Batista-Brito, R., Vinck, M., Ferguson, K.A., Chang, J.T., Laubender, D., Lur, G., Mossner, J.M., Hernandez, V.G., Ramakrishnan, C., Deisseroth, K., Higley, M.J., & Cardin, J.A. (2017) Developmental Dysfunction of VIP Interneurons Impairs Cortical Circuits. *Neuron*, **95**, 884-895.e9.

Benda, J., Longtin, A., & Maler, L. (2006) A synchronization-desynchronization code for natural communication signals. *Neuron*, **52**, 347–358.

Betterton, R.T., Broad, L.M., Tsaneva-Atanasova, K., & Mellor, J.R. (2017) Acetylcholine modulates gamma frequency oscillations in the hippocampus by activation of muscarinic M1 receptors. *Eur J Neurosci*, **45**, 1570–1585.

Bhattacharyya, A., Veit, J., Kretz, R., Bondar, I., & Rainer, G. (2013) Basal forebrain activation controls contrast sensitivity in primary visual cortex. *BMC Neurosci*, **14**, 55.

Bosman, C.A., Schoffelen, J.-M., Brunet, N., Oostenveld, R., Bastos, A.M., Womelsdorf, T., Rubehn, B., Stieglitz, T., De Weerd, P., & Fries, P. (2012) Attentional Stimulus Selection through Selective Synchronization between Monkey Visual Areas. *Neuron*, **75**, 875–888.

Brainard, D.H. (1997) The Psychophysics Toolbox. *Spat Vis*, **10**, 433–436.

596 Bressler, S.L. & Freeman, W.J. (1980) Frequency analysis of olfactory system EEG in cat, rabbit, and rat.
597 *Electroencephalogr Clin Neurophysiol*, **50**, 19–24.

598 Brunet, N., Vinck, M., Bosman, C.A., Singer, W., & Fries, P. (2014) Gamma or no gamma, that is the
599 question. *Trends Cogn Sci*, **18**, 507–509.

600 Bryant, A.S., Goddard, C.A., Huguenard, J.R., & Knudsen, E.I. (2015) Cholinergic Control of Gamma
601 Power in the Midbrain Spatial Attention Network. *Journal of Neuroscience*, **35**, 761–775.

602 Buzsáki, G. & Draguhn, A. (2004) Neuronal oscillations in cortical networks. *Science*, **304**, 1926–1929.

603 Buzsáki, G. & Wang, X.-J. (2012) Mechanisms of Gamma Oscillations. *Annual Review of Neuroscience*,
604 **35**, 203–225.

605 Cardin, J.A., Carlén, M., Meletis, K., Knoblich, U., Zhang, F., Deisseroth, K., Tsai, L.-H., & Moore, C.I.
606 (2009) Driving fast-spiking cells induces gamma rhythm and controls sensory responses. *Nature*, **459**,
607 663–667.

608 Chalk, M., Herrero, J.L., Gieselmann, M.A., Delicato, L.S., Gotthardt, S., & Thiele, A. (2010) Attention
609 Reduces Stimulus-Driven Gamma Frequency Oscillations and Spike Field Coherence in V1. *Neuron*, **66**,
610 114–125.

611 Chen, G., Zhang, Y., Li, X., Zhao, X., Ye, Q., Lin, Y., Tao, H.W., Rasch, M.J., & Zhang, X. (2017)
612 Distinct Inhibitory Circuits Orchestrate Cortical beta and gamma Band Oscillations. *Neuron*, **96**, 1403-
613 1418.e6.

614 Colgin, L.L., Denninger, T., Fyhn, M., Hafting, T., Bonnevie, T., Jensen, O., Moser, M.-B., & Moser, E.I.
615 (2009) Frequency of gamma oscillations routes flow of information in the hippocampus. *Nature*, **462**,
616 353–357.

617 Cone, J.J., Scantlen, M.D., Histed, M.H., & Maunsell, J.H.R. (2019) Different Inhibitory Interneuron Cell
618 Classes Make Distinct Contributions to Visual Contrast Perception. *eNeuro*, **6**.

619 Dipoppa, M., Ranson, A., Krumin, M., Pachitariu, M., Carandini, M., & Harris, K.D. (2018) Vision and
620 Locomotion Shape the Interactions between Neuron Types in Mouse Visual Cortex. *Neuron*, **98**, 602-
621 615.e8.

622 Dudai, A., Yayon, N., Lerner, V., Tasaka, G., Deitcher, Y., Gorfine, K., Niederhoffer, N., Mizrahi, A.,
623 Soreq, H., & London, M. (2020) Barrel cortex VIP/ChAT interneurons suppress sensory responses in
624 vivo. *PLOS Biology*, **18**, e3000613.

625 Eckenstein, F. & Baughman, R.W. (1984) Two types of cholinergic innervation in cortex, one co-
626 localized with vasoactive intestinal polypeptide. *Nature*, **309**, 153–155.

627 Friedrich, J., Zhou, P., & Paninski, L. (2017) Fast online deconvolution of calcium imaging data. *PLoS*
628 *Comput Biol*, **13**, e1005423.

629 Fries, P. (2009) Neuronal Gamma-Band Synchronization as a Fundamental Process in Cortical
630 Computation. *Annual Review of Neuroscience*, **32**, 209–224.

631 Fries, P. (2015) Rhythms for Cognition: Communication through Coherence. *Neuron*, **88**, 220–235.

632 Fries, P., Reynolds, J.H., Rorie, A.E., & Desimone, R. (2001) Modulation of oscillatory neuronal
633 synchronization by selective visual attention. *Science*, **291**, 1560–1563.

634 Fu, Y., Tucciarone, J.M., Espinosa, J.S., Sheng, N., Darcy, D.P., Nicoll, R.A., Huang, Z.J., & Stryker,
635 M.P. (2014) A Cortical Circuit for Gain Control by Behavioral State. *Cell*, **156**, 1139–1152.

636 Gieselmann, M.A. & Thiele, A. (2008) Comparison of spatial integration and surround suppression
637 characteristics in spiking activity and the local field potential in macaque V1. *European Journal of*
638 *Neuroscience*, **28**, 447–459.

639 Granger, A.J., Wang, W., Robertson, K., El-Rifai, M., Zanello, A.F., Bistrong, K., Saunders, A., Chow,
640 B.W., Nuñez, V., Turrero García, M., Harwell, C.C., Gu, C., & Sabatini, B.L. (2020) Cortical ChAT+
641 neurons co-transmit acetylcholine and GABA in a target- and brain-region-specific manner. *eLife*, **9**,
642 e57749.

643 Gray, C.M., Koenig, P., Engel, A.K., & Singer, W. (1989) Oscillatory responses in cat visual cortex
644 exhibit inter-columnar synchronization which reflects global stimulus properties. *Nature*, **338**, 334–337.

645 Hakim, R., Shamardani, K., & Adesnik, H. (2018) A neural circuit for gamma-band coherence across the
646 retinotopic map in mouse visual cortex. *eLife*, **7**.

647 Hasenstaub, A., Otte, S., & Callaway, E. (2016) Cell Type-Specific Control of Spike Timing by Gamma-
648 Band Oscillatory Inhibition. *Cereb Cortex*, **26**, 797–806.

649 Hasenstaub, A., Shu, Y., Haider, B., Kraushaar, U., Duque, A., & McCormick, D.A. (2005) Inhibitory
650 Postsynaptic Potentials Carry Synchronized Frequency Information in Active Cortical Networks. *Neuron*,
651 **47**, 423–435.

652 Hermes, D., Miller, K.J., Wandell, B.A., & Winawer, J. (2015) Stimulus Dependence of Gamma
653 Oscillations in Human Visual Cortex. *Cereb Cortex*, **25**, 2951–2959.

654 Hoseini, M.S., Higashikubo, B., Cho, F.S., Chang, A.H., Clemente-Perez, A., Lew, I., Ciesielska, A.,
655 Stryker, M.P., & Paz, J.T. (2021) Gamma rhythms and visual information in mouse V1 specifically
656 modulated by somatostatin+ neurons in reticular thalamus. *Elife*, **10**.

657 Howe, W.M., Gritton, H.J., Lusk, N.A., Roberts, E.A., Hetrick, V.L., Berke, J.D., & Sarter, M. (2017)
658 Acetylcholine Release in Prefrontal Cortex Promotes Gamma Oscillations and Theta-Gamma Coupling
659 during Cue Detection. *J Neurosci*, **37**, 3215–3230.

660 Jackson, J., Ayzenshtat, I., Karnani, M.M., & Yuste, R. (2016) VIP+ interneurons control neocortical
661 activity across brain states. *J Neurophysiol*, **115**, 3008–3017.

662 Jasper, H. & Penfield, W. (1949) Electrocorticograms in man: Effect of voluntary movement upon the
663 electrical activity of the precentral gyrus. *Arch. F. Psychiatr. U. Z. Neur.*, **183**, 163–174.

664 Karnani, M.M., Jackson, J., Ayzenshtat, I., Hamzehei Sichani, A., Manoocheri, K., Kim, S., & Yuste, R.
665 (2016) Opening Holes in the Blanket of Inhibition: Localized Lateral Disinhibition by VIP Interneurons.
666 *Journal of Neuroscience*, **36**, 3471–3480.

667 Karnani, M.M., Jackson, J., Ayzenshtat, I., Tucciarone, J., Manoocheri, K., Snider, W.G., & Yuste, R.
668 (2016) Cooperative Subnetworks of Molecularly Similar Interneurons in Mouse Neocortex. *Neuron*, **90**,
669 86–100.

670 Keller, A.J., Dipoppa, M., Roth, M.M., Caudill, M.S., Ingrosso, A., Miller, K.D., & Scanziani, M. (2020)
671 A Disinhibitory Circuit for Contextual Modulation in Primary Visual Cortex. *Neuron*, **108**.

Keller, A.J., Roth, M.M., & Scanziani, M. (2020) Feedback generates a second receptive field in neurons of the visual cortex. *Nature*, **582**, 545–549.

Lee, S., Kruglikov, I., Huang, Z.J., Fishell, G., & Rudy, B. (2013) A disinhibitory circuit mediates motor integration in the somatosensory cortex. *Nature Neuroscience*, **16**, 1662–1670.

Letzkus, J.J., Wolff, S.B.E., Meyer, E.M.M., Tovote, P., Courtin, J., Herry, C., & Lüthi, A. (2011) A disinhibitory microcircuit for associative fear learning in the auditory cortex. *Nature*, **480**, 331–335.

Lewis, D.A., Curley, A.A., Glausier, J.R., & Volk, D.W. (2012) Cortical parvalbumin interneurons and cognitive dysfunction in schizophrenia. *Trends Neurosci*, **35**, 57–67.

Lewis, D.A., Hashimoto, T., & Volk, D.W. (2005) Cortical inhibitory neurons and schizophrenia. *Nat Rev Neurosci*, **6**, 312–324.

Long, M.A., Jutras, M.J., Connors, B.W., & Burwell, R.D. (2005) Electrical synapses coordinate activity in the suprachiasmatic nucleus. *Nat Neurosci*, **8**, 61–66.

Lutzenberger, W., Pulvermüller, F., Elbert, T., & Birbaumer, N. (1995) Visual stimulation alters local 40-Hz responses in humans: an EEG-study. *Neurosci Lett*, **183**, 39–42.

Mathalon, D.H. & Sohal, V.S. (2015) Neural Oscillations and Synchrony in Brain Dysfunction and Neuropsychiatric Disorders: It's About Time. *JAMA Psychiatry*, **72**, 840–844.

Millman, D.J., Ocker, G.K., Caldejon, S., Kato, I., Larkin, J.D., Lee, E.K., Luviano, J., Nayan, C., Nguyen, T.V., North, K., Seid, S., White, C., Lecoq, J., Reid, C., Buice, M.A., & de Vries, S.E. (2020) VIP interneurons in mouse primary visual cortex selectively enhance responses to weak but specific stimuli. *eLife*, **9**, e55130.

Mitra, P. & Bokil, H. (2007) *Observed Brain Dynamics*, Observed Brain Dynamics. Oxford University Press.

Mossing, D.P., Veit, J., Palmigiano, A., Miller, K.D., & Adesnik, H. (2021) Antagonistic inhibitory subnetworks control cooperation and competition across cortical space (preprint). BioRxiv.

Mossner, J.M., Batista-Brito, R., Pant, R., & Cardin, J.A. (2020) Developmental loss of MeCP2 from VIP interneurons impairs cortical function and behavior. *Elife*, **9**.

Murty, D.V.P.S., Shirhatti, V., Ravishankar, P., & Ray, S. (2018) Large Visual Stimuli Induce Two Distinct Gamma Oscillations in Primate Visual Cortex. *The Journal of Neuroscience*, **38**, 2730–2744.

Neske, G.T. & Connors, B.W. (2016) Synchronized gamma-frequency inhibition in neocortex depends on excitatory-inhibitory interactions but not electrical synapses. *J Neurophysiol*, **116**, 351–368.

Niell, C.M. & Stryker, M.P. (2010) Modulation of Visual Responses by Behavioral State in Mouse Visual Cortex. *Neuron*, **65**, 472–479.

Nienborg, H., Hasenstaub, A., Nauhaus, I., Taniguchi, H., Huang, Z.J., & Callaway, E.M. (2013) Contrast Dependence and Differential Contributions from Somatostatin- and Parvalbumin-Expressing Neurons to Spatial Integration in Mouse V1. *Journal of Neuroscience*, **33**, 11145–11154.

Pachitariu, M., Stringer, C., Dipoppa, M., Schröder, S., Rossi, L.F., Dalgleish, H., Carandini, M., & Harris, K.D. (2017) Suite2p: beyond 10,000 neurons with standard two-photon microscopy. *bioRxiv*, 061507.

Pakan, J.M., Lowe, S.C., Dylda, E., Keemink, S.W., Currie, S.P., Coutts, C.A., & Rochefort, N.L. (2016) Behavioral-state modulation of inhibition is context-dependent and cell type specific in mouse visual cortex. *Elife*, **5**.

Perrenoud, Q., Pennartz, C.M.A., & Gentet, L.J. (2016) Membrane Potential Dynamics of Spontaneous and Visually Evoked Gamma Activity in V1 of Awake Mice. *PLOS Biology*, **14**, e1002383.

Peter, A., Uran, C., Klon-Lipok, J., Roese, R., van Stijn, S., Barnes, W., Dowdall, J.R., Singer, W., Fries, P., & Vinck, M. (2019) Surface color and predictability determine contextual modulation of V1 firing and gamma oscillations. *Elife*, **2019**, 38.

Pfeffer, C.K., Xue, M., He, M., Huang, Z.J., & Scanziani, M. (2013) Inhibition of inhibition in visual cortex: the logic of connections between molecularly distinct interneurons. *Nature Neuroscience*, **16**, 1068–1076.

Pi, H.-J., Hangya, B., Kvitsiani, D., Sanders, J.I., Huang, Z.J., & Kepecs, A. (2013) Cortical interneurons that specialize in disinhibitory control. *Nature*, **503**, 521–524.

Pluta, S., Naka, A., Veit, J., Telian, G., Yao, L., Hakim, R., Taylor, D., & Adesnik, H. (2015) A direct translaminar inhibitory circuit tunes cortical output. *Nature Neuroscience*, **18**, 1631–1640.

Pluta, S.R., Lyall, E.H., Telian, G.I., Ryapolova-Webb, E., & Adesnik, H. (2017) Surround Integration Organizes a Spatial Map during Active Sensation. *Neuron*, **94**, 1220-1233.e5.

Ray, S. & Maunsell, J.H.R. (2010) Differences in Gamma Frequencies across Visual Cortex Restrict Their Possible Use in Computation. *Neuron*, **67**, 885–896.

Ray, S. & Maunsell, J.H.R. (2011) Different Origins of Gamma Rhythm and High-Gamma Activity in Macaque Visual Cortex. *PLoS Biology*, **9**, e1000610.

Ray, S. & Maunsell, J.H.R. (2015) Do gamma oscillations play a role in cerebral cortex? *Trends in Cognitive Sciences*, **19**, 78–85.

Ray, S., Ni, A.M., & Maunsell, J.H.R. (2013) Strength of Gamma Rhythm Depends on Normalization. *PLoS Biology*, **11**, e1001477.

Riehle, A., Gruen, S., Diesmann, M., & Aertsen, A. (1997) Spike Synchronization and Rate Modulation Differentially Involved in Motor Cortical Function. *Science*, **278**, 1950–1953.

Saleem, A.B., Lien, A.D., Krumin, M., Haider, B., Rosón, M.R., Ayaz, A., Reinhold, K., Busse, L., Carandini, M., & Harris, K.D. (2017) Subcortical Source and Modulation of the Narrowband Gamma Oscillation in Mouse Visual Cortex. *Neuron*, **93**, 315–322.

Schnitzler, A. & Gross, J. (2005) Normal and pathological oscillatory communication in the brain. *Nature Reviews Neuroscience*, **6**, 285–296.

Sedley, W. & Cunningham, M.O. (2013) Do cortical gamma oscillations promote or suppress perception? An under-asked question with an over-assumed answer. *Frontiers in Human Neuroscience*, **7**.

Self, M.W., Peters, J.C., Possel, J.K., Reithler, J., Goebel, R., Ris, P., Jeurissen, D., Reddy, L., Claus, S., Baayen, J.C., & Roelfsema, P.R. (2016) The Effects of Context and Attention on Spiking Activity in Human Early Visual Cortex. *PLOS Biology*, **14**, e1002420.

Siegle, J.H., Pritchett, D.L., & Moore, C.I. (2014) Gamma-range synchronization of fast-spiking

interneurons can enhance detection of tactile stimuli. *Nature Neuroscience*, **17**, 1371–1379.

Sohal, V.S. & Huguenard, J.R. (2005) Inhibitory coupling specifically generates emergent gamma oscillations in diverse cell types. *Proc Natl Acad Sci U S A*, **102**, 18638–18643.

Sohal, V.S., Zhang, F., Yizhar, O., & Deisseroth, K. (2009) Parvalbumin neurons and gamma rhythms enhance cortical circuit performance. *Nature*, **459**, 698–702.

Storchi, R., Bedford, R.A., Martial, F.P., Allen, A.E., Wynne, J., Montemurro, M.A., Petersen, R.S., & Lucas, R.J. (2017) Modulation of Fast Narrowband Oscillations in the Mouse Retina and dLGN According to Background Light Intensity. *Neuron*, **93**, 299–307.

Tallon, C., Bertrand, O., Bouchet, P., & Pernier, J. (1995) Gamma-range activity evoked by coherent visual stimuli in humans. *Eur J Neurosci*, **7**, 1285–1291.

Traub, R.D., Bibbig, A., LeBeau, F.E.N., Buhl, E.H., & Whittington, M.A. (2004) Cellular mechanisms of neuronal population oscillations in the hippocampus in vitro. *Annu Rev Neurosci*, **27**, 247–278.

Traub, R.D., Kopell, N., Bibbig, A., Buhl, E.H., LeBeau, F.E., & Whittington, M.A. (2001) Gap junctions between interneuron dendrites can enhance synchrony of gamma oscillations in distributed networks. *J Neurosci*, **21**, 9478–9486.

Tukker, J.J., Fuentealba, P., Hartwich, K., Somogyi, P., & Klausberger, T. (2007) Cell type-specific tuning of hippocampal interneuron firing during gamma oscillations in vivo. *J Neurosci*, **27**, 8184–8189.

Uhlhaas, P.J. & Singer, W. (2010) Abnormal neural oscillations and synchrony in schizophrenia. *Nat Rev Neurosci*, **11**, 100–113.

van Kerkoerle, T., Self, M.W., Dagnino, B., Gariel-Mathis, M.-A., Poort, J., van der Togt, C., & Roelfsema, P.R. (2014) Alpha and gamma oscillations characterize feedback and feedforward processing in monkey visual cortex. *Proceedings of the National Academy of Sciences*, **111**, 14332–14341.

Veit, J., Hakim, R., Jadi, M.P., Sejnowski, T.J., & Adesnik, H. (2017) Cortical gamma band synchronization through somatostatin interneurons. *Nature Neuroscience*, **20**, 951–959.

Vinck, M., van Wingerden, M., Womelsdorf, T., Fries, P., & Pennartz, C.M.A. (2010) The pairwise phase consistency: A bias-free measure of rhythmic neuronal synchronization. *NeuroImage*, **51**, 112–122.

Vinck, M., Womelsdorf, T., Buffalo, E.A., Desimone, R., & Fries, P. (2013) Attentional modulation of cell-class-specific gamma-band synchronization in awake monkey area v4. *Neuron*, **80**, 1077–1089.

Wall, N.R., De La Parra, M., Sorokin, J.M., Taniguchi, H., Huang, Z.J., & Callaway, E.M. (2016) Brain-Wide Maps of Synaptic Input to Cortical Interneurons. *J Neurosci*, **36**, 4000–4009.

Wehr, M. & Laurent, G. (1996) Odour encoding by temporal sequences of firing in oscillating neural assemblies. *Nature*, **384**, 162–166.

Womelsdorf, T. & Fries, P. (2006) Neuronal coherence during selective attentional processing and sensory-motor integration. *J Physiol Paris*, **100**, 182–193.

Wulff, P., Ponomarenko, A.A., Bartos, M., Korotkova, T.M., Fuchs, E.C., Bähner, F., Both, M., Tort, A.B.L., Kopell, N.J., Wisden, W., & Monyer, H. (2009) Hippocampal theta rhythm and its coupling with gamma oscillations require fast inhibition onto parvalbumin-positive interneurons. *Proc Natl Acad Sci U S A*, **106**, 3561–3566.

Xu, X. & Callaway, E.M. (2009) Laminar Specificity of Functional Input to Distinct Types of Inhibitory Cortical Neurons. *Journal of Neuroscience*, **29**, 70–85.

Yizhar, O., Fenno, L.E., Prigge, M., Schneider, F., Davidson, T.J., O'Shea, D.J., Sohal, V.S., Goshen, I., Finkelstein, J., Paz, J.T., Stehfest, K., Fudim, R., Ramakrishnan, C., Huguenard, J.R., Hegemann, P., & Deisseroth, K. (2011) Neocortical excitation/inhibition balance in information processing and social dysfunction. *Nature*, **477**, 171–178.

Zhang, S., Xu, M., Kamigaki, T., Hoang Do, J.P., Chang, W.-C., Jenvay, S., Miyamichi, K., Luo, L., & Dan, Y. (2014) Long-range and local circuits for top-down modulation of visual cortex processing. *Science*, **345**, 660–665.

Zhang, Z., Russell, L.E., Packer, A.M., Gauld, O.M., & Häusser, M. (2018) Closed-loop all-optical interrogation of neural circuits in vivo. *Nat Methods*, **15**, 1037–1040.

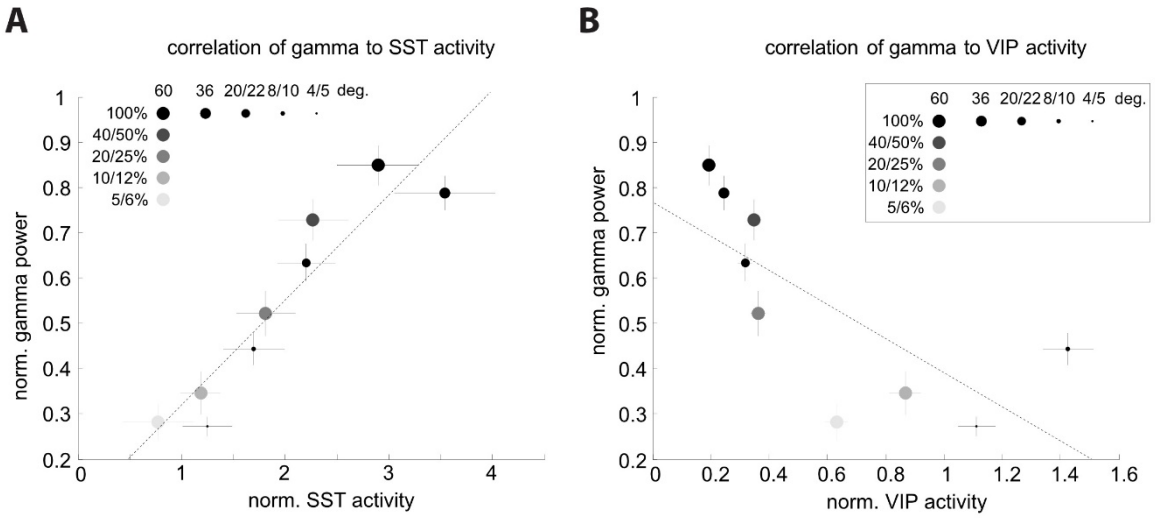

Figure 4, Suppl 1. VIP neuron activity is anti-correlated to gamma power during quiescence. A: Plot of averaged normalized gamma power vs. averaged normalized SST-cell activity (deconvolved event-rate/mean) while the animal was quiescent, recorded via 2-photon imaging in a different set of animals across similar conditions. Different shades of gray represent different stimulus contrast and different symbol sizes represent different stimulus sizes. Dashed line is a linear fit of the data. SST-cell activity is strongly correlated to gamma power ($r(7) = 0.93$, $p<0.001$). **B:** Same as A, except for normalized VIP cell activity. VIP activity is strongly anti-correlated to gamma power ($r(7) = -0.73$, $p = 0.024$).

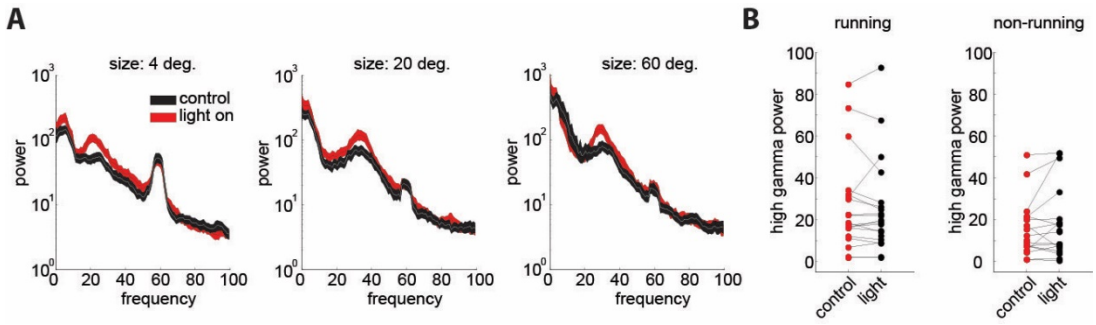

Figure 5 Suppl 1. Effects of VIP inactivation on higher-frequency, narrowband, thalamic gamma (60Hz). A: Spectra for different size grating stimuli with (red) and without (black) inactivation of VIP neurons. VIP affects the visually induced 30Hz gamma band, but not the thalamically relayed 60Hz gamma band that is supressed by large/high contrast stimuli. **B:** Plot comparing the LFP high gamma band power for blank stimuli in the running condition for control (black) and light (red) trials (n = 19, p = 0.33, Wilcoxon signed rank test) Right: Plot comparing the LFP high gamma band power for blank stimuli in the non-running condition for control (black) and light (red) trials (n = 18, p = 0.25, Wilcoxon signed rank test).

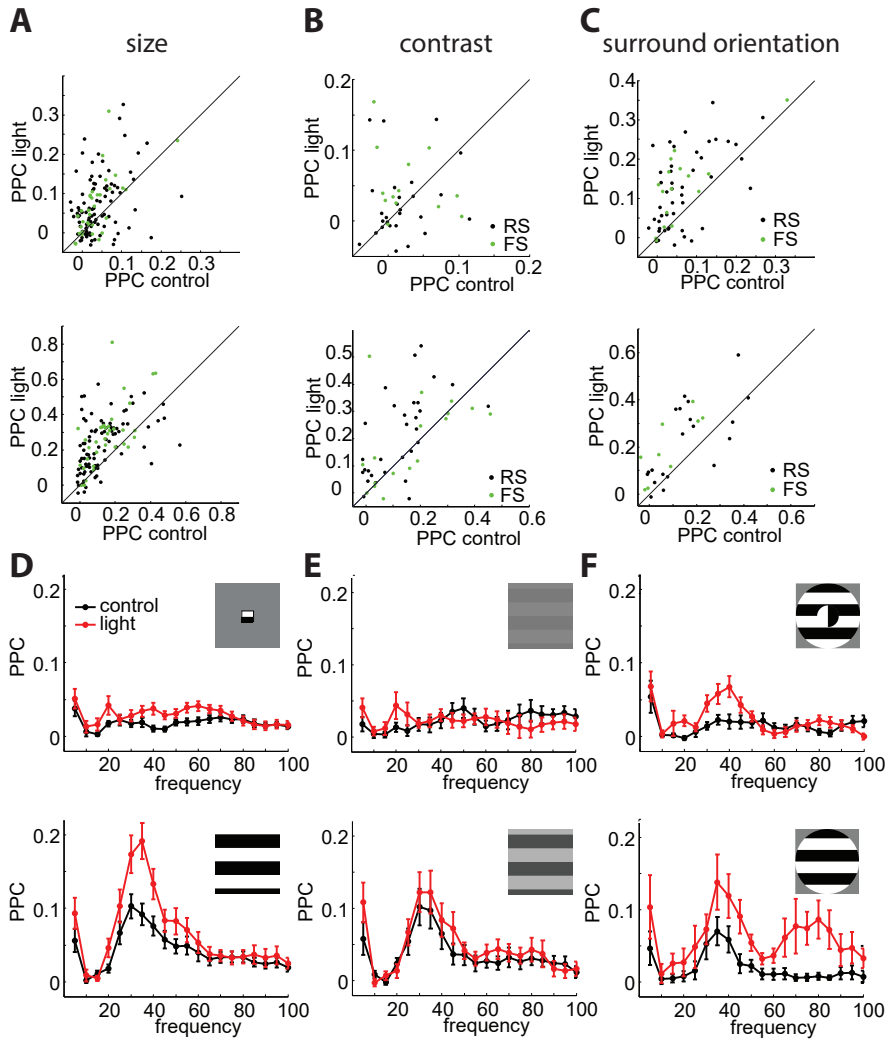

Fig. 6, Suppl 1. Effects of VIP inactivation on locking of single RS and FS cells. A: Top: scatter plot of PPC values for single RS (black, n = 90, p = 0.0001, Wilcoxon signed rank test) and FS (green, n = 33, p = 0.002, Wilcoxon signed rank test) cells in response to small (4˚) stimuli in control condition versus VIP suppression. Bottom: scatter plot of PPC values for single RS (black, n = 87, p = 0.0004, Wilcoxon signed rank test) and FS (green, n = 35, p = 0.002, Wilcoxon signed rank test) cells in response to large (60˚) stimuli in control condition versus VIP suppression. **B:** Top: scatter plot of PPC values for single RS (black, n = 27, p = 0.61, Wilcoxon signed rank test) and FS (green, n = 13, p = 0.31, Wilcoxon signed rank test) cells in response to low contrast (5%) stimuli in control condition versus VIP suppression. Bottom: scatter plot of PPC values for single RS (black, n = 30, p = 0.001, Wilcoxon signed rank test) and FS (green, n = 17, p = 0.98, Wilcoxon signed rank test) cells in response to large (60˚) stimuli in control condition versus VIP suppression. **C:** Top: scatter plot of PPC values for single RS (black, n = 46, p < 0.0001, Wilcoxon signed rank test) and FS (green, n = 15, p = 0.0006, Wilcoxon signed rank test) cells in response to cross surround stimuli in control condition versus VIP suppression.Bottom: scatter plot of PPC values for single RS (black, n = 21, p = 0.04, Wilcoxon signed rank test) and FS (green, n = 9, p = 0.004, Wilcoxon signed rank test) cells in response to iso surround (0˚ offset) stimuli in control condition versus VIP suppression. **D:** Top: average PPC spectra for L2/3 FS cells with (red) and without (black) suppression of VIP cells (n = 30) for small (4˚) stimuli. Bottom: average PPC spectra for L2/3 FS cells with (red) and without (black) suppression of VIP cells (n = 32) for large (60˚) stimuli. **E:** Top: average PPC spectra for L2/3 FS cells with (red) and without (black) suppression of VIP cells (n = 13) for low contrast (5%) stimuli. Bottom: average PPC spectra for L2/3 FS cells with (red) and without (black) suppression of VIP cells (n = 17) for high contrast (80%) stimuli. **F:** top: average PPC spectra for L2/3 FS cells with (red) and without (black) suppression of VIP cells (n = 15) for cross surround (90˚ offset) stimuli. Bottom: average PPC spectra for L2/3 FS cells with (red) and without (black) suppression of VIP cells (n = 9) for iso surround (0˚ offset) stimuli.

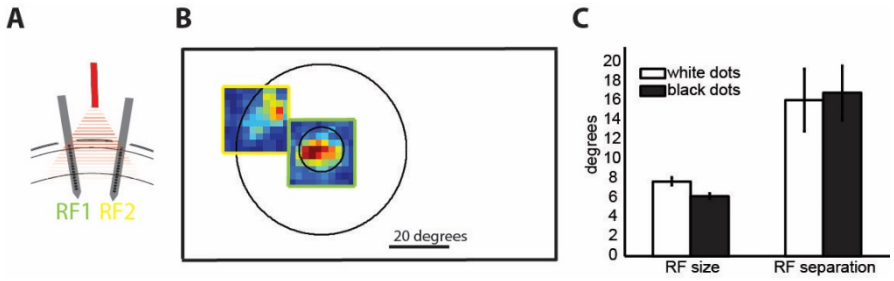

Figure 8, Suppl 1. Receptive field mapping procedure for coherence measurement. A: Schematic of the multielectrode array recording configuration with two laminar arrays in distant sites (530+-90 µm apart, histology from n = 7 mice) corresponding to two separate retinotopic locations (RF1 (green) and RF2 (yellow), 15° ± 3° of visual angle separation, n = 11 mice). Red triangle denotes wide illumination with optogenetic light delivered from a fiber located above the two recording sites. **B:** Two sparse noise mapped RFs (redder colors denote higher firing rates), one from electrode 1 (green frame), one from electrode 2 (yellow frame) superimposed on the outline of the center and surround of the visual stimulus used for the coherence analysis (Figure 7). Large outer frame is approximately the size of the stimulation monitor. **C:** average RF size (2 standard deviations of Gaussian fit to RF) and average separation of center and surround fields, separately for fields mapped with white and black sparse noise, n = 8.